



Comparison of probabilistic multivariate wind environment between typhoon and synoptic climate and its propagation in buffeting response for a long-span bridge

Peng Liu ^{a,b}, Wei Cui ^{a,b,c,*}, Lin Zhao ^{a,b,c,d}

^a State Key Lab of Disaster Reduction in Civil Engineering, Tongji University, Shanghai 200092, China

^b Department of Bridge Engineering, College of Civil Engineering, Tongji University, Shanghai 200092, China

^c Key Laboratory of Transport Industry of Wind Resistant Technology for Bridge Structures, Tongji University, Shanghai 200092, China

^d State Key Laboratory of Featured Metal Materials and Life-cycle Safety for Composite Structures, Guangxi University, Nanning 530004, China

ARTICLE INFO

Keywords:

Probabilistic wind spectrum
Parameter correlation modeling
Probabilistic propagation
Buffeting response
Multi-outputs

ABSTRACT

Buffeting of bridges is turbulence-induced vibration affecting the serviceability and may lead to structural fatigue. The first step in evaluating the buffeting response is to determine the turbulence parameters in the wind environment based on field measurements. For long-span bridges in coastal regions, both typhoon and synoptic wind climates attack the bridge sites. In this study, the multiparameter dependence of turbulence parameters under typhoon and synoptic wind climates is established employing the isoprobabilistic transformation method. A surrogate model based on polynomial chaos expansion is then constructed from the transformed isoprobabilistic model to estimate the vertical, lateral and torsional buffeting responses at multiple locations on the bridge. Compared to synoptic winds, typhoons exhibit higher turbulence intensity and greater dispersion in turbulence parameters. The turbulence spectrum of typhoons shows higher energy in the lower frequency range. The multivariable turbulence parameters are modeled using the Gaussian Copula. For bridge buffeting, typhoons cause higher response amplitudes even at the same wind speed as synoptic winds. Additionally, the vertical and torsional responses exhibit nonlinear dependencies, particularly at high wind speeds.

1. Introduction

As the span of bridges has increased rapidly over the past decade, wind-induced vibrations have become a primary concern in the structural design of long-span bridges. Normally, the time series of wind speed can be decomposed into an average component U and turbulence components, including the along wind components $u(t)$, lateral wind speed $v(t)$ and vertical wind component $w(t)$ based on the three directions orthogonal to the mean wind direction. All three turbulence components are assumed to follow the Gaussian distribution with zero mean.

Traditionally, research on the wind environment is primarily about synoptic wind climate. Parameters characterizing the wind field of the atmospheric boundary layer under synoptic wind are measured through anemometers and analyzed with statistical methods [1,2]. The mean wind profile describes the variation of mean wind speed with vertical elevation in the atmospheric boundary layer and can be represented by the power law or logarithmic law. Turbulence intensity, a dimensionless factor, is defined as the standard deviation of turbulence components divided by the mean wind speed. It is generally assumed to

be constant and is primarily related to surface roughness and elevation above the ground. The turbulence length scale characterizes turbulence coherence, referring to the average size of the larger eddies in turbulent flow [3]. The turbulence wind spectrum describes the distribution of turbulence energy across different frequencies or wavelengths and can be represented by the von Kármán wind spectrum. For synoptic winds, the mean wind direction remains relatively constant, and the movement of air masses is stable, resulting in minimal variability in wind parameters. The average measured values of wind turbulence parameters have been incorporated into several regional wind loading codes [4,5].

Currently, newly constructed infrastructure is increasingly located in coastal or offshore areas due to economic development, exposing these structures to more frequent typhoons [6–8]. Given the distinctive characteristics of the vortex wind field in a typhoon climate, near-ground wind characteristics differ significantly from those in other synoptic climate models [9]. Researchers universally acknowledge that the design wind speeds of a typhoon should be higher [10]. However, because large samples of high-frequency typhoon wind records are

* Correspondence to: 320 Wind Engineering Building, Tongji University, 1239 Siping Road, Shanghai, 200092, China.

E-mail addresses: 1550008@tongji.edu.cn (P. Liu), cuiwei@tongji.edu.cn (W. Cui), zhaolin@tongji.edu.cn (L. Zhao).

not available, the statistical characteristics of wind turbulence during typhoons remain unclear [11–13]. For example, the special wind profiles of typhoons cannot be described by the logarithmic law [14,15]. Turbulence intensity values are higher than synoptic winds at a similar mean wind speed [16–18]. In addition, the energy of the turbulent wind spectrum at low frequencies is higher than that of synoptic wind and cannot be accurately described by the von Kármán spectrum, particularly near the typhoon eye [18,19]. However, the limited availability of observational data often restricts the statistical analysis of typhoon turbulence to a single typhoon or a few events, limiting its application in engineering applications.

For significant infrastructure, the probability distribution of wind-induced response is required rather than the deterministic approach. Therefore, the probability description of turbulence parameters in both typhoons and synoptic wind is necessary. Traditionally, for synoptic winds, the distribution of turbulence parameters is analyzed individually on the based on univariate statistics.

Furthermore, the mutual correlation among turbulence parameters are analyzed. For example, Fenerci et al. [20] and Liu et al. [21] established a dependence relationship between the turbulence parameters and the mean wind speed based on extensive wind environment data collected through the health monitoring system of both bridges. However, current analysis procedures primarily focus on the relationship between turbulence parameters and wind speed, often neglecting the correlations among the turbulence parameters themselves.

The Copula function based on Skalar's theory [22] is a powerful tool for establishing the joint distribution [23]. Many studies have used Copula-based joint distribution for bivariate analyses of wind environment parameters, such as wind speed and direction [24], wind speed and temperature [25]. Trivariate analyses, such as those involving wind speed, direction, and angle of attack [26], have also been conducted, revealing strong correlations among wind environment parameters in synoptic climates.

The above research primarily focuses on the synoptic climate in the monitoring area, with a limited number of analyzed turbulence parameters, leaving the correlations among other wind environment parameters insufficiently explored. Therefore, it is necessary to develop the multiparameters (>3) joint probability distribution model to investigate the turbulence characters of both typhoon and synoptic climates.

After establishing the joint distribution of turbulence parameters, the most straightforward approach to evaluate the buffeting response or failure probability under a target statistical return period is to randomly sample from the input turbulence parameter space and calculate the corresponding response using a computational model, commonly referred to as the Monte Carlo (MC) simulation method. However, MC methods require numerous calls to the computational model, which incurs substantial CPU costs [27]. To improve the efficiency of response probability evaluation, two approaches are commonly referenced in related works. The first is to derive the environmental contour (EC) [28] for a given recurrence period by combining the joint probability distribution of environmental variables, then obtain the extreme response along the EC. This method reduces the number of computational model calls and has been successfully used by Lystad to evaluate buffeting responses [29,30]. The second approach is to reduce the computational cost of each model call by establishing a surrogate model based on a finite number of computations. This study adopts the latter method to improve the efficiency of response evaluation and facilitate response propagation.

Surrogate models, such as Kriging (Gaussian process regression), sequential Gaussian process [31], neural networks (NN), and polynomial chaos expansion (PCE) [32], are employed to estimate the propagation of uncertainty from wind turbulence parameters to wind-induced vibrations. Typically, a surrogate model approximates a computational model exhibiting finite variance using a mathematical function. Kriging is a nonparametric model that relies on the correlation structure of

data points, assuming a Gaussian process prior over the unknown function and utilizing covariance functions (kernel functions) to model the spatial correlation between points. This method has been widely applied in wind-induced vibration analysis [33] and structural reliability evaluation [32,34]. However, its computational demands increase significantly with larger datasets or higher-dimensional input spaces, mainly due to the computation and inversion of covariance matrices. Neural networks build the mapping relationship between input and output through the weights and biases of neurons [35]. In general, both Kriging and neural networks are implicit black-box methods that require additional interpretation to understand their underlying mechanics.

The PCE approximates computational models using a set of orthogonal basis functions based on the distribution space of input variables or data-driven arbitrary basis functions derived from statistical moments [36]. The coefficients are determined through projection or regression methods [37,38]. The PCE provides a polynomial representation of the model, offering greater interpretability compared to other surrogate models, although it may be slightly less accurate than the Kriging method when applied to high-dimensional data.

One of the main challenges is that surrogate models typically require input variables to follow independent and specific probability distributions [39]. Liu et al. [40] expressed the distribution of turbulence parameters in terms of mean and variance as functions of mean wind speed, employing multipoint estimation and the maximum entropy method to establish the probability propagation from turbulence parameters to structural response. However, the correlation between turbulence parameters is not adequately addressed in the current literature.

This study addresses the issue from two perspectives. First, using 12 years of monitoring data, a probabilistic multiparameter correlation model is developed for wind turbulence in the contexts of both typhoons and synoptic winds. The work evaluates the disparities in the correlation model between these two distinct climates. Second, the Gaussian Copula-based Nataf transformation is applied to convert the turbulence parameter space into an independent standard Gaussian space. Using a PCE surrogate model, the study establishes the probability propagation of the multiparameter correlation model, assessing its impact on wind-induced vibrations in the structure under both typhoon and synoptic wind conditions. Additionally, considering the multi-objective output, the correlation of wind-induced responses across different sections and degrees of freedom of the main beam is evaluated. This research provides valuable insights into the differences in turbulence parameter correlations during typhoons versus favorable weather conditions, the influence of multiparameter inputs on structural response, and the evaluation of structural responses at multiple critical sections.

2. Methodology

2.1. General concept

The Performance-Based approach for the assessment of risk under wind action has been a main method for the entire process analysis of wind-induced vibration in the last two decades [41]. Wind environment variables are the first part of the wind loading chain [42], and the foundation of performance-based wind resistance design lies in evaluating the most unfavorable load conditions and their probability of occurrence [20,43]. However, the dependence of non-synoptic wind characteristics such as typhoon cannot be confused with synoptic wind. Based on the statistical analysis of the measured wind data, probabilistic models under different climate are established. The dependence between turbulence parameters may be complex, and its influence on structural wind-induced vibration is still unclear. Direct simulation by finite element model is limited by the cost of multiple calls to the structural model [29]. Therefore, the research focuses on analyzing the

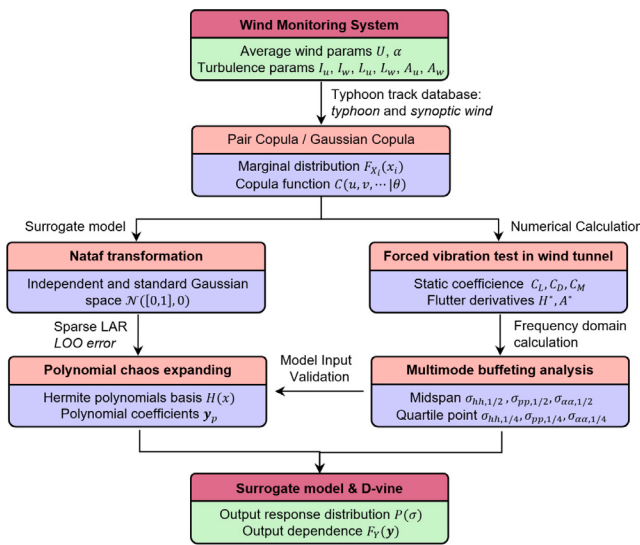


Fig. 1. Flowchart for probabilistic wind environment and its propagation in multi-output in buffeting.

similarities and differences of the turbulence parametric dependence between the typhoon and synoptic wind, in addition, briefly exploring the differences of their probability distribution after propagating to the structural response by surrogate model. Accordingly, the bullet points and implementation methods of this study are as follows:

- Statistical wind parameters: a variety of wind characteristics, including average wind parameters and turbulence parameters, affect the structural response. The wind parameters of the long-term monitoring wind data are obtained.
- Probabilistic modeling: The probabilistic correlation model for synoptic wind and typhoon parameters should be established to adequately reflect the dependence among these turbulence parameters by the Copula theory.
- Multimode buffeting analysis: combined with the finite element method and Scanlan's aerodynamic theory, the modal superposition method is used to calculate the wind-induced response of the long-span suspension bridge along the span in the frequency domain.
- Nataf transformation: using the Nataf transformation [44], the probabilistic multiparameter space of the wind characteristics is transformed into an independent parameter space subject to the standard distribution since the dependence since the multi-variable probabilistic model cannot meet the independent requirements of the input space of the surrogate model.
- Polynomial chaos expanding: a PCE surrogate model is constructed in the standard space sample to realize the probabilistic propagation of multivariable wind environment probability space to multipoint wind-induced response.
- Response probability analysis: Monte Carlo simulation is used to calculate the probability of wind-induced response on the surrogate model and analyze the correlation of multi-output response by D-vine Copula.

The procedure described above is summarized in Fig. 1 to illustrate each step of the above methodologies.

2.2. Wind data characteristics

2.2.1. Mean wind speed

From the time series recording of the wind monitoring sensors, the raw wind speeds include three components $u_x(t), u_y(t)$ and $u_z(t)$ pointing

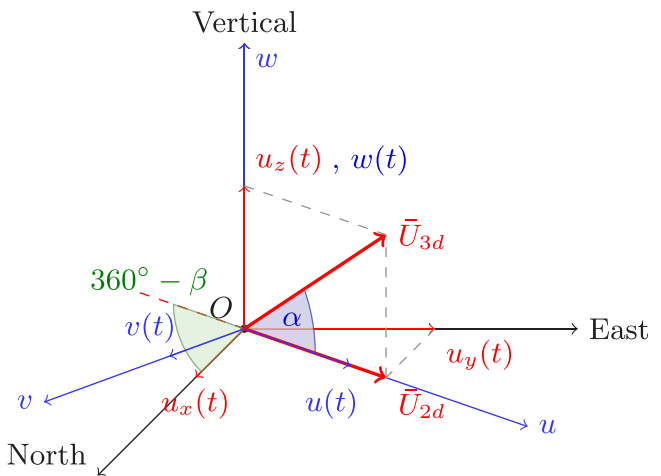


Fig. 2. Composition and decomposition of wind speed recorded by ultrasonic anemometers.

north, east and vertical direction, respectively (shown in Fig. 2). The wind speed time series can be decomposed into the mean wind speed U_{2d} and U_{3d} along the main wind direction and three mutually perpendicular turbulence components $u(t), v(t)$, and $w(t)$. The corresponding 10-min mean wind speed can be expressed as:

$$\begin{aligned} U_{2d} &= \sqrt{\bar{u}_x(t)^2 + \bar{u}_y(t)^2} \\ U_{3d} &= \sqrt{\bar{u}_x(t)^2 + \bar{u}_y(t)^2 + \bar{u}_z(t)^2} \end{aligned} \quad (1)$$

where $\bar{u}_a(t) = \frac{1}{N} \sum_{i=1}^N u_a(t)$, ($a = x, y, z$); N denotes the number of sampling points within 10-min averaging interval.

2.2.2. Mean wind direction

Based on Fig. 2, the mean wind direction β (unit: $^\circ$) can be expressed in Eq. (2).

$$\beta = \arccos\left(\frac{\bar{u}_x(t)}{U_{2d}}\right) \quad (2)$$

where $\beta = 0^\circ$ and $\beta = 180^\circ$ represent the north and the south direction, respectively. Therefore, the orthogonal turbulence wind speed components (along-wind $u(t)$, lateral $v(t)$, vertical $w(t)$) dependent on the mean wind direction can be expressed as:

$$\begin{aligned} u(t) &= u_x(t) \cos(\beta) + u_y(t) \sin(\beta) - U_{2d} \\ v(t) &= u_x(t) \sin(\beta) - u_y(t) \cos(\beta) \\ w(t) &= u_z(t) \end{aligned} \quad (3)$$

2.2.3. Angles of attack

And the angles of attack (AoAs) α (unit: $^\circ$) can be expressed as:

$$\alpha = \arctan\left(\frac{\bar{w}(t)}{U_{2d}}\right) \quad (4)$$

2.2.4. Turbulence intensity

The standard deviations (STD) of three turbulence wind speed components are important parameters representing turbulence wind intensity, which can be expressed as:

$$\sigma_a = \sqrt{\frac{1}{N} \sum_{i=1}^N [a(t) - \bar{a}(t)]^2}, \quad a = u, v, w \quad (5)$$

When σ_a is normalized by the mean wind speed (U_{2d}), the resulting wind characteristic is turbulence intensity, denoted as I_a :

$$I_a = \frac{\sigma_a}{U_{2d}}, \quad a = u, v, w \quad (6)$$

2.2.5. Turbulence length scale

The turbulence length scale is the average length of turbulent eddies, and different methods of calculating it also give significantly different results. Theoretically, the turbulence scale is defined as follows.

$$L_a = \frac{U_{2d}}{\sigma_a^2} \int_0^\infty R_a(\tau) d\tau \quad (7)$$

where $R_a(\tau)$ is the auto-correlation of each velocity component, u , v , w . In this study, to get a consistent estimation of the turbulence length scale, the auto-correlation function $R_a(\tau)$ is integrated numerically from $\tau = 0$ to the first crossing of $R_a(\tau) = 0$.

2.2.6. Turbulence wind spectrum

The turbulent wind spectrum, also known as the power spectral density (PSD) of turbulence, is a key characteristic of the wind environment, used to describe the energy distribution of turbulence in the frequency domain. The wind power spectrum within the atmospheric boundary layer is assumed to follow Kolmogorov's hypothesis [42]. This theory posits that energy is transferred from larger-scale eddies to smaller-scale eddies through inertial mechanisms, with dissipation occurring at an equal rate due to viscous effects in a steady flow. The primary mechanism for energy dissipation occurs within extremely small-scale eddies. According to Buckingham's theory [45], the decreasing slope of the normalized wind spectrum with respect to a reduced frequency in the inertial subregion should follow a $-5/3$ decay rate.

Many previous studies [21,46] have shown that Kaimal-form spectra can well fit the trend of distribution of turbulence wind energy in the range of 0.01~4 Hz. The wind spectrum of the Kaimal form is as follows:

$$\frac{fS_a(f)}{\sigma_a^2} = \frac{A_a \frac{fL_a}{U}}{\left(1 + 1.5A_a \frac{fL_a}{U}\right)^{\frac{5}{3}}} \quad (8)$$

where A_a is the parameters to be fitting for each turbulence component ($a = u, v, w$); $S_a(f)$ is the PSD of a .

However, because of variations in data acquisition quality and the range of wind speeds, achieving a robust fit for all turbulence wind spectra is difficult. The observed PSD is calculated using Welch's method [47] with 25% length overlap and 50% length Hanning window function. The wind spectrum of the observed PSD is fitted according to the form of Eq. (8). The goodness of fit R^2 (Eq. (9)) serves as a metric to assess effectiveness. Fig. 3 shows the distribution of R^2 for all measurement data. To ensure the quality of the parameters fitted to the wind spectrum, the segments with $R^2 \geq 0.7$ are considered as validation observational data for the variables of the wind environment. Associated with the transition in the eyewall layer between complex convection and sheared eddies produced by the low-level jet [19], the wind spectrum of Kaimal-form has a slightly better fitting effect on the synoptic wind than typhoon. For typhoons, 70.5% of the data is eliminated, and 59.3% for synoptic winds.

$$R^2 = 1 - \frac{SS_{res}}{SS_{tot}} \quad (9)$$

where SS_{res} is the residual sum of squares (the sum of squares for the differences between fitting values and actual observations), and SS_{tot} is the total sum of square (the sum of squares for the differences between actual observations and their mean).

Fig. 4 illustrates the spectrum diagram showcasing the fitted turbulence wind spectra of all observed sample points during typhoons with respect to mean wind speed. The Kaimal-form wind spectrum succinctly encapsulates the distribution of turbulent energy across various mean wind speed ranges.

According to the above statistical parameters of the wind environment that affect the structural wind-induced response, the multi-parameter space involved in this study will include the mean wind speed U , angle of attack α , turbulence intensity along the wind I_u , vertical turbulence intensity I_w , turbulence length scale along the wind L_u , vertical turbulence length scale L_w , Kaimal-form along-wind wind spectral parameter A_u , and vertical Kaimal wind spectral parameter A_w , a total of eight variables.

Table 1

Bi-variate copula used in this study: Φ is the uni-variate standard normal distribution; $\Phi_{z,\theta}$ is the bi-variate normal distribution with zero means, unit variances, and correlation parameter θ ; t_v is the uni-variate t distribution with v degrees of freedom, and $t_{v,\theta}$ is the bi-variate t distribution with v degrees of freedom and correlation parameter θ .

Name	$C(u, v; \theta)$	Parameter range
Independence	uv	
Gaussian	$\Phi_{2,\theta}(\Phi^{-1}(u), \Phi^{-1}(v))$	$\theta \in (-1, 1)$
Clayton	$(u^{-\theta} + v^{-\theta} - 1)^{-1/\theta}$	$\theta > 0$
Gumbel	$\exp(-((-\log u)^\theta + (-\log v)^\theta)^{1/\theta})$	$\theta \in [1, +\infty]$
Frank	$-\frac{1}{\theta} \log\left(\frac{1-e^{-\theta u}-(1-e^{-\theta u})(1-e^{-\theta v})}{1-e^{-\theta v}}\right)$	$\theta \in (-\infty, 0) \cup (0, +\infty)$
t	$t_{2:v,\theta}(t_v^{-1}(u), t_v^{-1}(v))$	$v > 1, \theta \in (-1, 1)$

2.3. Multiparameters probability model for wind turbulence

2.3.1. Marginal distribution for each turbulence parameter

Determining the marginal distribution for each turbulence parameter is the fundamental step for the following dependency analysis of the wind turbulence parameters. The probability density function (PDF) and the cumulative distribution function (CDF) can be used to describe a random parameter. The Gaussian, Lognormal, Gumbel, Gamma, Weibull, and Laplace distributions are the most common in this subject. Table A.1 in Appendix A displays their parameters, PDF, and CDF.

2.3.2. Bivariate copula

The most straightforward and convenient method for assessing the correlation between two variables is to examine the magnitude of the correlation coefficient. However, in the majority cases, relying solely on the correlation coefficient is insufficient and may ignore some important information. The copula function is a valuable tool for linking the marginal distributions of random variables with the joint distribution function. At the basis of the copula formalism lies on Sklar's theorem [22], for any M -variate distribution F_X of an $X = [X_1, \dots, X_M]$ with marginals cumulative distribution function F_{X_1}, \dots, F_{X_M} , there exists a copula C such that

$$F_X(x) = C(F_{X_1}(x_1), F_{X_2}(x_2), \dots, F_{X_M}(x_M)) \quad (10)$$

From Eq. (10), the joint probability density function (PDF) of X is obtained by differentiation:

$$f_X(x) = c(F_{X_1}(x_1), F_{X_2}(x_2), \dots, F_{X_M}(x_M)) \prod_{i=1}^M f_{X_i}(x_i) \quad (11)$$

where f_{X_i} is the marginals PDF; and $c(\cdot)$ is the copula density function obtained as

$$c(u_1, \dots, u_M) = \frac{\partial^M C(u_1, \dots, u_M)}{\partial u_1 \cdots \partial u_M} \quad (12)$$

There are several copula families available to characterize the dependency relationships between bivariate random variables ($M = 2$). Copula families account for diverse dependency structures between binary variables, including tail dependencies. In this investigation, particular emphasis is placed on the Gaussian Copula, t Copula, and the Archimedean Copula family (like Clayton, Gumbel, and Frank copula). Each copula within these families possesses a distinct generating function, taking the following form:

Table 1 presents a number of copula functions, each with a corresponding relevant scene and a parameter selection range. When two random variables are independent, the joint distribution function can be constructed directly using the independence copula. The Gaussian copula is grounded in the multivariate Gaussian distribution, making it suitable for linear correlations, with dependence measured by the

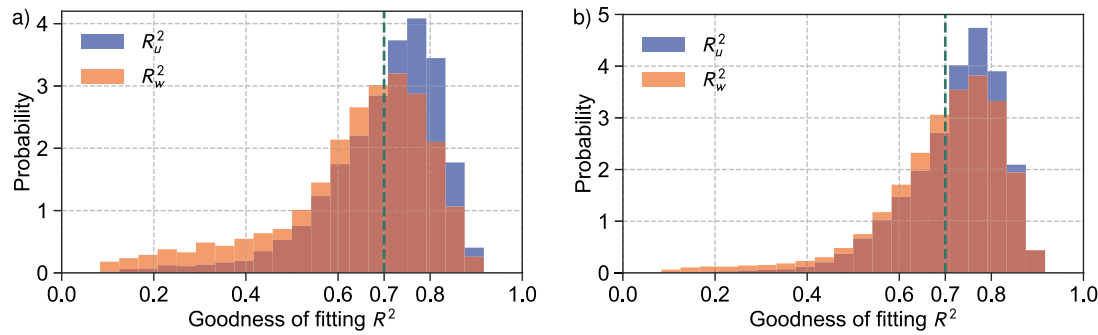


Fig. 3. Goodness of fitting for Kaimal form wind spectrum: (a) typhoon, (b) synoptic wind.

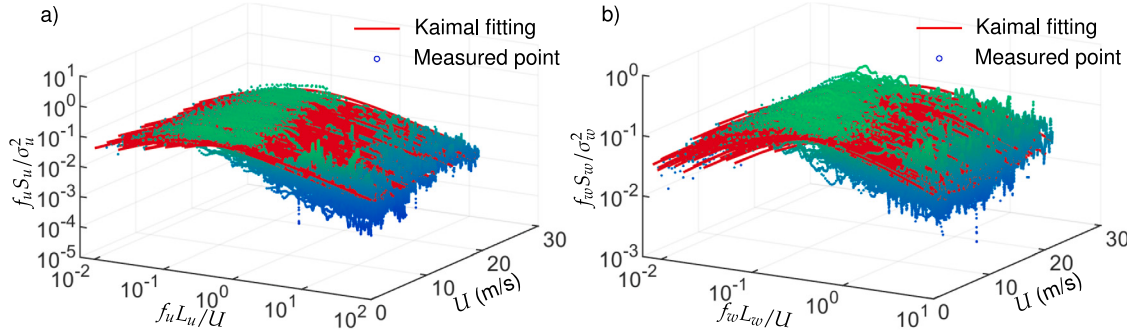


Fig. 4. Kaimal-type fitting of the turbulence wind spectrum: (a) along-wind, (b) vertical.

Pearson correlation coefficient. The Clayton copula is adept at simulating positive correlations, particularly in scenarios with pronounced tail correlations [48]. The Gumbel copula is used to simulate robust tail correlations and is generally better suited for extreme value distributions [49]. The Frank copula exhibits versatility, which makes it applicable for simulating a variety of dependencies [50]. The t copula is well suited to handle peaked and thick-tailed distributions, allowing the incorporation of tail dependencies within dependent structures [51].

It should be emphasized that the above bi-variate copula functions are all symmetric, and it is a relevant preliminary step to check if their underlying bivariate copula is symmetry. Formally, if the underlying copula is symmetry, the below upper bound formula for bivariate empirical copula should be satisfied:

$$n_\infty(\hat{C}) = \sup_{(u_1, u_2) \in [0,1]^2} \{|\hat{C}(u_1, u_2) - \hat{C}(u_2, u_1)|\} = 0 \quad (13)$$

where the \hat{C} denotes the empirical copula function, which can be estimated by a natural nonparametric method introduced by Rüschenhoff [52]:

$$\hat{C}(u_1, u_2) = \frac{1}{n} \text{Card} \left[(U_1, U_2) | U_1 \leq u_1, U_2 \leq u_2 \right] \quad (14)$$

where the U_i is the pseudo observation of cumulative distribution function and the rank based method is adopted here.

However, the symmetry in Eq. (13), which deals with the deterministic upper bound of the discrete empirical copula function, is only a theoretical concept, so the method of hypothesis testing [53] is used to verify its symmetry. The zero hypothesis is given by:

$$\mathbb{H}_0 : \hat{C}(u_1, u_2) = \hat{C}(u_2, u_1), \forall (u_1, u_2) \in (0, 1)^2 \quad (15)$$

2.3.3. Multi-variate copula

Although the copula families described in Table 1 hold for the generating functions $M > 2$, their form is not unique. Common copulas include the Gaussian copula and vine construction by the product of possibly conditional pair copulas. The form of the multivariable Gaussian copula function is based on the multidimensional Gaussian joint

distribution, similar to the form of the pair copula, and the parameters of the copula function depend on the multivariate Pearson correlation coefficient.

The vine copula was first introduced by Bedford and Cook [54]. The idea of conditional probability is adopted to construct a multivariable joint distribution, whose joint PDF can be expressed by the following formula referred to Eq. (11)

$$c(F_{X_1}(x_1), F_{X_2}(x_2), \dots, F_{X_M}(x_M)) \prod_{i=1}^M f_{X_i}(x_i) \\ = \prod_{j=1}^M f_{j|j+1,\dots,M}(x_j|x_{j+1}, \dots, x_M). \quad (16)$$

That is, the right-hand side can be rewritten as a product of conditional pair copulas multiply by marginal CDF $\prod_i F_{X_i}(x_i)$, and the joint copula for multivariable ($M > 2$) is expressed as a product of pair copulas, such as $M - 1$ unconditional pair copulas, $M - 2$ pair copulas conditioned on 1 variable, \dots , and 1 pair copula conditioned on $M - 2$ variables for a total of $M(M - 2)/2$ pair copulas. The canonical (C-) vine and drawable (D-) vine are two classes of vine structures. In principle, there is no distinction between the two, and it can be decided on the basis of how well the building condition copula functions.

2.3.4. Inference and selection criteria

The maximum likelihood (ML) estimate is used to estimate the parameters θ of the marginals and their copula. The ML estimator of θ based on observations $\hat{X} = \{\hat{x}^{(1)}, \dots, \hat{x}^{(n)}\}$ is defined as

$$\hat{\theta} = \operatorname{argmax}_{\theta} \prod_{h=1}^n f_X(\hat{x}^{(h)}; \theta) \stackrel{\text{def}}{=} \operatorname{argmax}_{\theta} \mathcal{L}(\theta) \quad (17)$$

where the $\mathcal{L}(\theta)$ is the likelihood function.

For a set of observations, there are typically several parameter estimation distributions available to represent the distribution of the observed variables. However, ML estimation typically favors the fitting

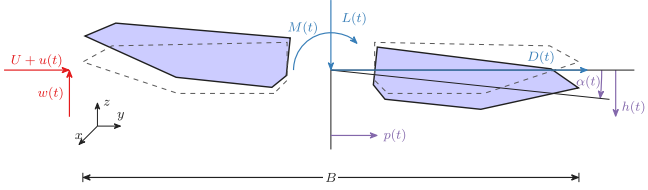


Fig. 5. Two coordinate system about aerodynamic force and bridge motion (The notations can be found in Eq. (24)).

distribution with the highest likelihood value, potentially leading to a preference for distributions with more parameters or copula.

To mitigate overfitting, the Akaike Information Criterion (AIC, Eq. (18)) and Bayesian Information Criterion (BIC, Eq. (19)) [55,56] are used to select the most appropriate distribution and copula function.

$$\text{AIC} = 2k - 2 \log(\mathcal{L}(\theta)) \quad (18)$$

$$\text{BIC} = \log(n)k - 2 \log(\mathcal{L}(\theta)) \quad (19)$$

where k is the number of modal parameters to be estimated and n is the number of samples. Among the two candidates, the one that provides the lowest values is selected to model the joint distribution [57].

2.4. Isoprobabilistic: Nataf transformation

Nataf is a method for transforming random variables and calculating the correlation distortion based on the Gaussian copula. Nataf transformation $T = T_2 \circ T_1 : X \rightarrow W$ can be divided into two steps: transforming an arbitrary marginal distribution into a standard normal distribution ($T_1 : X \rightarrow Z$); Transform the standard normal distribution into independent components ($T_2 : Z \rightarrow W$), where W obeys the independent standard Gaussian. According to Nataf transformation theory [58], an n -dimensional dependent random vector X for which the marginal CDF $F_{X_i}(x_i)$ and the correlation matrix $C_X = [\xi_{ij}]$ are known, can be transformed (component-wise) to standard Gaussian random vector $Z = [Z_1, \dots, Z_n]$ with correlation matrix $C_Z = [\rho_{ij}]$ through the transformation:

$$T_1 : X_i \rightarrow Z_i = \Phi^{-1}(F_i(X_i)) \sim \mathcal{N}([0, 1]) \quad (20)$$

where $\Phi(\cdot)$ is the standard Gaussian CDF; $\mathcal{N}([0, 1])$ is the standard Gaussian distribution; and $Z \sim \mathcal{N}([0, 1], C_Z)$.

This transformation caused a correlation distortion; the correlation coefficient between standard normal variables Z_i and Z_j , denoted ρ_{ij} , is not equal to its counterpart in the parameter space ($\rho_{ij} \neq \xi_{ij}$).

If the Gaussian correlation ρ_{ij} is known, the non-Gaussian correlation ξ_{ij} can be determined through the following integral equation:

$$\xi_{ij} = \frac{1}{\sigma_{X_i} \sigma_{X_j}} \int_{-\infty}^{\infty} \int_{-\infty}^{\infty} (X_i - \mu_{X_i})(X_j - \mu_{X_j}) \phi_2(Z_i, Z_j; \rho_{ij}) dZ_i dZ_j \quad (21)$$

where $X_i = F_{X_i}^{-1}(\Phi(Z_i))$ and $\phi_2(\cdot)$ is the bivariate standard normal probability density function. The integration is directly evaluated using a two-dimensional quadratic Gauss-Legendre integration. However, in the case where the non-Gaussian correlation is known ξ_{ij} , the above integral cannot be inverted to solve for the Gaussian correlation ρ_{ij} . In such a case, iterative methods must be employed, such as the Iterative Translation Approximation Method (ITAM).

To obtain the standard Gaussian and independent components W , the Cholesky factor L of C_Z is adopted:

$$C_Z = LL^T \quad (22)$$

therefore, W can be given in

$$T_2 : Z \rightarrow W = L^{-1}Z \sim \mathcal{N}([0, 1], \mathbf{0}) \quad (23)$$

By Nataf transformation T , the multi-parameters of the wind environment, when modeled with a Gaussian copula, can be transformed into a set of independent standard normal random variables [9]. The Nataf transformation also has its corresponding inverse transformation form, which is not detailed here.

2.5. Buffeting theory for multimode analysis in frequency domain

Buffeting of bridges is a type of stochastic vibration caused by self-excited forces and stochastic turbulent wind loads. The governing equation of bridge deck motion for a continuum structure is typically expressed as:

$$M\ddot{d} + C\dot{d} + Kd = F_{se} + F_b \quad (24)$$

where M , C and K are the mass, damping and stiffness matrices, respectively; d is the motion array consisting of the displacement at three degrees of freedom (DOFs): horizontal p , vertical h and rotation α . For the long-span bridge, the node force vector F consists of a self-motion-excited aeroelastic force F_{se} and a random aerodynamic force induced by turbulence F_b . Both have three direction components corresponding to the DOFs: drag force D_{se} and D_b , lift force L_{se} and L_b , and M_{se} and M_b .

Fig. 5 illustrates the external force and motion per span in the bridge section.

For a linear superposition system, the motion of the bridge deck is represented in terms of the generalized coordinate of the mode $\eta_i(t)$ and the dimensionless modal values of the i th mode along the deck $h_i(x)$, $p_i(x)$ and $\alpha_i(x)$

$$\begin{aligned} p(x, t) &= \sum_i p_i(x) B \eta_i(t) \\ h(x, t) &= \sum_i h_i(x) B \eta_i(t) \\ \alpha(x, t) &= \sum_i \alpha_i(x) \eta_i(t) \end{aligned} \quad (25)$$

If the bridge section vibrates in harmonic motion, the self-excited forces are commonly described by Scanlan's flutter derivatives:

$$\begin{aligned} D_{se} &= \frac{1}{2} \rho U^2 B \left(\kappa P_1^* \frac{\dot{p}}{U} + \kappa P_2^* \frac{B \dot{\alpha}}{U} + \kappa^2 P_3^* \alpha + \kappa^2 P_4^* \frac{p}{B} + \kappa P_5^* \frac{\dot{h}}{U} \right. \\ &\quad \left. + \kappa^2 P_6^* \frac{h}{B} \right) \\ L_{se} &= \frac{1}{2} \rho U^2 B \left(\kappa H_1^* \frac{\dot{h}}{U} + \kappa H_2^* \frac{B \dot{\alpha}}{U} + \kappa^2 H_3^* \alpha + \kappa^2 H_4^* \frac{h}{B} + \kappa H_5^* \frac{\dot{p}}{U} \right. \\ &\quad \left. + \kappa^2 H_6^* \frac{p}{B} \right) \\ M_{se} &= \frac{1}{2} \rho U^2 B^2 \left(\kappa A_1^* \frac{\dot{h}}{U} + \kappa A_2^* \frac{B \dot{\alpha}}{U} + \kappa^2 A_3^* \alpha + \kappa^2 A_4^* \frac{h}{B} + \kappa A_5^* \frac{\dot{p}}{U} \right. \\ &\quad \left. + \kappa^2 A_6^* \frac{p}{B} \right) \end{aligned} \quad (26)$$

where ρ is air density; U is the mean wind speeds; $\kappa = \omega B/U$ is the reduced frequency; B is the bridge deck width; ω is the circular frequency; H_i^* , P_i^* and A_i^* ($i = 1 \sim 6$) are frequency dependent flutter derivatives.

The turbulence-dependent buffeting forces F_b per unit span are normally expressed as:

$$\begin{aligned} D_b(t) &= \frac{1}{2} \rho U^2 B \left(2C_D \chi_{D_{bu}} \frac{u(t)}{U} + C'_D \chi_{D_{bw}} \frac{w(t)}{U} \right) \\ L_b(t) &= \frac{1}{2} \rho U^2 B \left(2C_L \chi_{L_{bu}} \frac{u(t)}{U} + (C'_L + C_D) \chi_{L_{bw}} \frac{w(t)}{U} \right) \\ M_b(t) &= \frac{1}{2} \rho U^2 B^2 \left(2C_M \chi_{M_{bu}} \frac{u(t)}{U} + C'_M \chi_{M_{bw}} \frac{w(t)}{U} \right) \end{aligned} \quad (27)$$

where C_L , C_D , C_M are the mean lift, drag, and moment coefficients, respectively; $C'_L = dC_L/d\alpha$, $C'_D = dC_D/d\alpha$ and $C'_M = dC_M/d\alpha$; $\chi_{L_{bu}}$, $\chi_{D_{bu}}$, $\chi_{D_{bw}}$, $\chi_{M_{bu}}$ and $\chi_{D_{bw}}$ are the aerodynamic transfer function between turbulence wind velocities and buffeting force (aerodynamic admittance). These are a function of frequency and depend on the aerodynamic configuration of the deck.

$$\phi_i(x) = \begin{pmatrix} p_i(x)B \\ h_i(x)B \\ \alpha_i(x) \end{pmatrix} \quad (28)$$

$$I_{ij} = \int_0^l \phi_i(x)\phi_j(x)dm(x) \quad (29)$$

where $dm(x)$ denotes infinitesimal inertia.

Substituted Eq. (26) and (27) into Eq. (24), and taking Fourier transform, the governing equation can be transformed into the reduced frequency κ domain and written simply

$$E\bar{\eta} = \bar{Q}_b \quad (30)$$

where E and \bar{Q}_b is an $n \times n$ matrix; n is the number of structural modal orders considered. Each element of the E matrix can be represented as:

$$E_{ij}(\kappa) = I_{ij}[-\kappa^2 + i(2\kappa_i\zeta_i\kappa - C_{se,ij}) + (\kappa_i^2 - K_{se,ij})] \quad (31)$$

where $i^2 = -1$; ζ_i is the damping ratio of girder; $\kappa_i = \omega_i B/U$; ω_i is the circular frequency of girder.

C_{se} and K_{se} are the aerodynamic damping matrix and the aerodynamic stiffness matrix caused by F_{se} , respectively. $C_{se,ij}$ can be given

$$C_{se,ij}(\kappa) = \int_0^l \frac{1}{2I_{ij}} \rho B^2 \kappa^2 \phi_j(x)^T \begin{pmatrix} P_1^* & P_5^* & BP_2^* \\ H_5^* & H_1^* & BH_2^* \\ BA_5^* & BA_1^* & B^2 A_2^* \end{pmatrix} \phi_i(x)dx \quad (32)$$

$$D_{se,ij}(\kappa) = \int_0^l \frac{1}{2I_{ij}} \rho B^2 \kappa^2 \phi_j(x)^T \begin{pmatrix} P_4^* & P_6^* & BP_3^* \\ H_6^* & H_4^* & BH_3^* \\ BA_6^* & BA_4^* & B^2 A_4^* \end{pmatrix} \phi_i(x)dx$$

The power spectral density (PSD) matrix for the generalized coordinate η is developed using standard random vibration theory

$$S_{\eta\eta}(\kappa) = E^{-1} S_{Q_b Q_b} [E^*]^{-1} \quad (33)$$

where E contains the structural inertia force, damping force, elastic recovery force, aerodynamic elastic force, and aerodynamic damping force; and E^* denotes the complex conjugate transpose of matrix E .

The PSD matrix of \bar{Q}_b can be expressed as

$$S_{Q_{bi} Q_{bj}}(\kappa) = \left(\frac{\rho B^3}{2U} \right)^2 \int_0^l \int_0^l \phi_i^T(x_1) \mathbf{B}_q(\kappa) \mathbf{S}_V(\Delta x, \kappa) \mathbf{B}_q^T(\kappa) \phi_j(x_2) dx_1 dx_2 \quad (34)$$

$$\mathbf{B}_q(\kappa) = \begin{pmatrix} 2C_D \chi_{D_{bu}} & C'_D \chi_{D_{bw}} \\ 2C_L \chi_{L_{bu}} & (C'_L + C_D) \chi_{L_{bu}} \\ 2C_M \chi_{M_{bu}} & C'_M \chi_{M_{bw}} \end{pmatrix} \quad (35)$$

$$\mathbf{S}_V(\Delta x, \kappa) = \begin{pmatrix} S_{uu}(\Delta x, \kappa) & S_{uw}(\Delta x, \kappa) \\ S_{uw}(\Delta x, \kappa) & S_{ww}(\Delta x, \kappa) \end{pmatrix} \quad (36)$$

where $S_{aa}(\Delta x, \kappa)$, $a = u, v, w$ is the cross-spectral density of turbulence at two points with the distance Δx . The off-diagonal terms are usually assumed to be negligible because of their insignificant influence on the dynamic vibration. Then, it can be rewritten as :

$$\mathbf{S}_V(\Delta x, \kappa) = \begin{pmatrix} S_u(\kappa) & 0 \\ 0 & S_w(\kappa) \end{pmatrix} \times \begin{pmatrix} C_u(\Delta x, \kappa) & 0 \\ 0 & C_w(\Delta x, \kappa) \end{pmatrix} \quad (37)$$

where $S_a(\kappa)$, $a = u, v, w$ is the one-point power spectrum densities and $C_a(\kappa)$, $a = u, v, w$ is the normalized cross-spectral densities for Δx .

As a result, the vertical, lateral and torsional ($^\circ$) root mean square (RMS) response of the girder located at x can be derived as:

$$\sigma_{hh} = \sqrt{\int_0^\infty B^2 \sum_i \sum_j h_i(x)h_j(x)S_{\eta\eta}(K)dK} \quad (38)$$

$$\sigma_{pp} = \sqrt{\int_0^\infty B^2 \sum_i \sum_j p_i(x)p_j(x)S_{\eta\eta}(K)dK}$$

$$\sigma_{aa} = \frac{180}{\pi} \sqrt{\int_0^\infty \sum_i \sum_j \alpha_i(x)\alpha_j(x)S_{\eta\eta}(K)dK}$$

2.6. Surrogate model: polynomial chaos expanding

The approach to establish probability propagation between input and output variables involves assessing uncertainty through statistical sampling methods, which typically includes Monte Carlo (MC) simulation and its derivatives. The convergence of MC method depends on the dimensions of the input variables. As dimensions increase, the complexity and computational requirements of the simulation generally increase. Although the implementation of MC method is simple and more direct, one disadvantage of MC cannot be ignored is that MC method usually requires to call the computational model during each simulation, and its computational cost limits its application in engineering. As the dimension of the variable increases, the efficiency benefits of the MC method are restricted because each simulation is still carried out using the computational model. To improve the efficiency of calling model, surrogate model represented by polynomial chaos expansion (PCE) method is widely used to estimate the probability transfer from input variable space to output variable space. The PCE emerges as a semi-analytical and semi-simulation uncertainty analysis method. Its core concept involves generating a set of complete orthogonal bases through the probability space of independent single variables within the random input probability space to approximate the output variable. By applying the fitted polynomial functions to replace the system model in the original problem, the efficiency of a single simulation is significantly enhanced. Through the aforementioned equal probability Nataf transformation, it becomes possible to achieve probability propagation from the multivariate dependent space of the wind environment to the probability space of the wind response. This facilitates the construction of a surrogate model under multi-objective output scenarios combined with Nataf transformation and PCE.

But, one limitation should be pointed out here is that the Nataf transformation is a Gaussian copula-based isoprobabilistic transformation method, and its input variable must meet the Gaussian distribution. In other words, the method is only applicable to considered variables with no significant tail dependence. In addition, PCE is also cursed by dimensionality [59], so after fitting the surrogate model, the cross-validation is needed to check its validity.

Considering multimode buffeting calculation in the frequency domain is to build a map $\mathbf{Y} = \mathcal{M}(\mathbf{X})$, the PCE model is to build polynomial functions to replace the \mathcal{M} :

$$\mathbf{Y} = \mathcal{M}(\mathbf{X}) = \sum_{p \in \mathbb{N}^M} y_p \Psi_p(\mathbf{X}) \quad (39)$$

where $\mathbf{Y} = [\sigma_{hh,1/2}, \sigma_{pp,1/2}, \sigma_{aa,1/2}, \sigma_{hh,1/4}, \sigma_{pp,1/4}, \sigma_{aa,1/4}]$ denotes the multi-output vector for vertical responses RMS at middle span ($\sigma_{hh,1/2}$), lateral response RMS at middle span ($\sigma_{pp,1/2}$), torsional responses RMS at middle span ($\sigma_{aa,1/2}$), vertical responses RMS at quartile span ($\sigma_{hh,1/4}$), lateral response RMS at middle span ($\sigma_{pp,1/4}$), and torsional responses RMS at quartile span ($\sigma_{aa,1/4}$); $\Psi_p(\mathbf{X})$ are the multivariate polynomial orthonormal with respect to f_X ; $p \in \mathbb{N}^M$ is a multi-index that identifies the components of the multivariate polynomial Ψ_p ; and $y_p \in \mathbb{R}$ are the corresponding coefficients. In realistic applications, the sum in Eq. (39) needs to be truncated to a finite sum for calculation efficiency, it should be truncated:

$$\widehat{\mathcal{M}}(\mathbf{X}) \approx \sum_{p \in \mathcal{A}} y_p \Psi_p(\mathbf{X}) \quad (40)$$

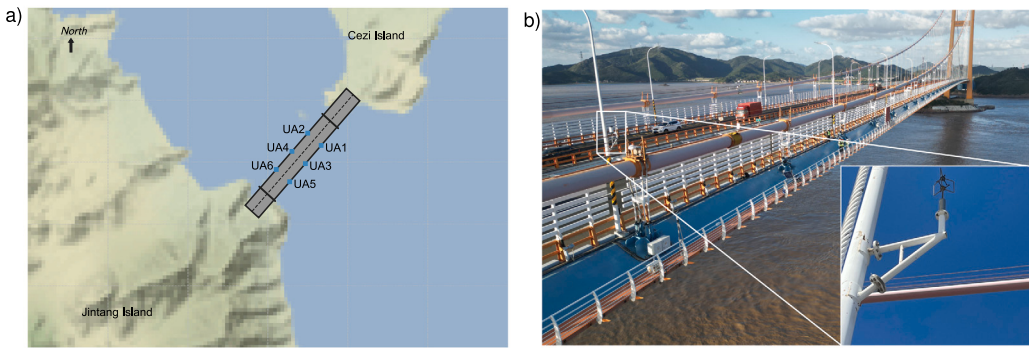


Fig. 6. Layout of ultrasonic anemometers: (a) location of wind sensors, (b) Sensor installation position (lamp post).

where $\mathcal{A} \in \mathbb{N}^M$ is the set of selected multi-index of multivariate polynomial; and $\widehat{\mathcal{M}}(\mathbf{X})$ denotes the estimation by surrogate model. To balance the relationship between accuracy and computational efficiency, the number of orthogonal bases is usually consistent with or close to the number of random variables M .

For the Gaussian distribution, the polynomial orthogonal to it is usually chosen as a Hermite polynomial. There are several methods for calculating the coefficients y_p of the PCE for a given basis. The sparse PCE (Least Angle Regression, LAR) [60,61] algorithm is used in this study. The relative training error is defined by:

$$\begin{aligned}\epsilon_{emp} &= \frac{Err_{emp}}{\hat{V}[\mathcal{Y}]} \\ Err_{emp} &= \frac{1}{N} \sum_{i=1}^N \left(y^{(i)} - \widehat{\mathcal{M}}(\mathbf{x}^{(i)}) \right)^2 \\ \hat{V}[\mathcal{Y}] &= \frac{1}{N-1} \sum_{i=1}^N \left(y^{(i)} - \bar{y} \right)^2\end{aligned}\quad (41)$$

where $\widehat{\mathcal{M}}(\mathbf{x}^{(i)})$ is the estimated values by PCE; N is the number of sampling points. In addition, the leave-one-out (LOO) cross-validation error is used to measure the generalization error of the surrogate model by v -fold cross-validation. More details on sparse LAR and error estimates can be found in this thesis [62].

3. Multi parameters wind correlation modeling for synoptic wind and typhoon

3.1. Description about engineering application example

The structural health monitoring system that monitors the wind information and structural response at the several sections of the bridge was installed in 2009 for the Xihoumen Bridge. The structural health monitoring system includes three-dimensional ultrasonic anemometers and unidirectional accelerometers. Young Model 81000 three-dimensional ultrasonic anemometers (UA) are used to monitor the wind speed of the bridge deck, at a sampling frequency $f_s = 32$ Hz. The ultrasonic anemometers are located on lighting poles (Fig. 6) on the side of the bridge girder at 1/4, 1/2 and 3/4 spans by cantilever trusses with enough vertical space to avoid interference effects. To mitigate interference from auxiliary structures, only sensor data from the windward side is utilized for a specific wind direction.

Xihoumen Bridge health monitoring system encompasses an extensive dataset of wind speed samples, including synoptic wind as well as those generated by typhoons. For the typhoon wind environment, the wind series is considered a typhoon when the nearest distance from the typhoon eye to the bridge site is less than 400 km. From 2009 to 2022, a total of 12 typhoons affected the Xihoumen Bridge, Muifa in 2011, Bolaven in 2012, Tembin in 2012, Kong-Rey in 2013, Fung-Wong in 2014, Meranti in 2016, Ampil in 2018, Jongdari in 2018, Danas in 2019, Lekima in 2019, Hagupit in 2020 and Muifa in 2022.

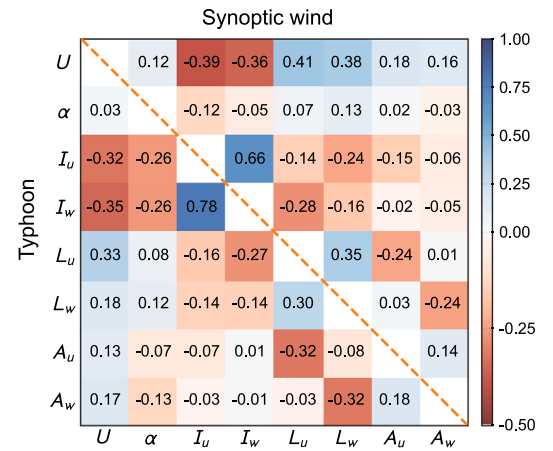


Fig. 7. Measure of association for Kendall's tau: lower triangle denotes typhoon, upper triangle denotes synoptic wind.

It is crucial to do a comprehensive examination of wind data within a sizable historical dataset and to compare the distinct dependence differences between winds caused by typhoons and normal weather winds in detail, which will play a crucial role in revealing the unique meteorological characteristics connected to typhoons.

3.2. Correlation coefficients of turbulence parameters

The correlation coefficient is one of the most intuitive indicators for reflected dependencies between variables. Various commonly used correlation coefficient indicators, including Pearson's r , Spearman's rho, and Kendall's tau, exhibit properties of measure of associate but are applicable in different contexts and scenarios based on specific needs. Compared with linear correlation (Pearson's r), the Kendall's tau measures the dependency between two variables, which is the difference between the probability of concordance and the probability of discordance between X_1 and X_2 :

$$\tau(X_1, X_2) = \mathbb{P}[(X_1 - X'_1)(X_2 - X'_2) > 0] - \mathbb{P}[(X_1 - X'_1)(X_2 - X'_2) < 0] \quad (42)$$

where (X_1, X_2) is a random vector, and (X'_1, X'_2) is an independent copy of (X_1, X_2) . A positive value of τ indicates that X_1 and X_2 are more likely to increase or decrease in unison. Kendall's tau measures the rank correlation between two variables, making it a more suitable choice regardless of whether the variables are linear or non-linear relationship. The Kendall's rank coefficient, illustrated in Fig. 7, is presented here as a concise measure to estimate the dependency between variables. To compare the difference in measure of association under two different wind environments, the lower triangle denotes Kendall's tau under typhoon, and the upper triangle denotes it under synoptic

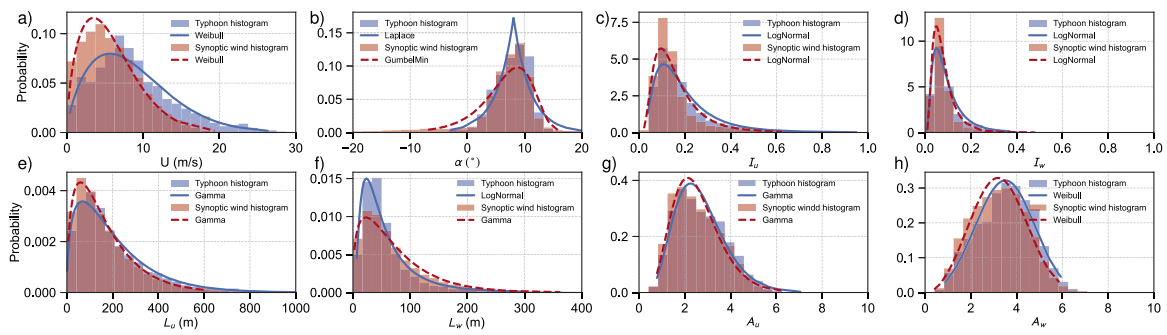


Fig. 8. Marginal distribution of wind characteristics: (a) mean wind speed, (b) angle of attack, (c) along-wind turbulence intensity, (d) vertical turbulence intensity, (e) along-wind turbulence length scale, (f) vertical turbulence length scale, (g) along-wind spectral parameter, (h) vertical spectral parameter.

Table 2
Goodness of fit of marginal distribution.

Typhoon	U	I_u	I_w	L_u	L_w	A_u	A_w
Normal	0.946	0.749	0.668	0.801	0.491	0.973	0.992
Lognormal	0.346	0.959	0.952	0.739	0.929	0.932	0.813
Gumbel-min	0.991	0.871	0.809	0.920	0.657	0.962	0.841
Weibull	0.997	0.916	0.882	0.978	0.794	0.982	0.925
Gamma	0.980	0.916	0.873	0.983	0.765	0.987	0.944
Synoptic wind	U	I_u	I_w	L_u	L_w	A_u	A_w
Normal	0.954	0.649	0.512	0.851	0.768	0.970	0.992
Lognormal	0.148	0.892	0.807	0.559	0.781	0.939	0.866
Gumbel-min	0.986	0.784	0.676	0.955	0.895	0.967	0.898
Weibull	0.996	0.851	0.764	0.994	0.969	0.991	0.998
Gamma	0.965	0.842	0.739	0.997	0.973	0.989	0.966

wind. The correlation between wind environment variables appears to be intricate. For example, the correlation coefficient between I_u and I_w is notably high. Moreover, the turbulence parameters are not solely dependent on the mean wind speed. For example, the turbulence length scales (L_u , L_w) exhibit a robust correlation with the mean wind speed. On the contrary, the Kaimal-form fitting parameters show a weaker association with mean wind speed U , but show a pronounced correlation with the turbulence length scales. This highlights the inadequacy of only establishing dependence between the turbulence parameters of the wind environment and the mean wind speed for a complete understanding. Differences in the dependence between typhoons and the synoptic wind are evident.

3.3. Marginal distribution for wind characteristics

To establish the dependency and probability model between typhoons and the synoptic wind, it is imperative to deduce the marginal distribution of the variables of the wind environment [63]. By incorporating the AIC penalty item evaluation criteria and goodness of fit R^2 (Table 2), the marginal distribution depicted in Fig. 8 was determined. The statistical moments of the measured value and the p -value of the Kolmogorov-Smirnov test (if $p > 0.05$, accept the distribution) [64] are presented in Table 3.

The marginal distribution in Fig. 8 reveals slight distinctions, particularly in the distribution of mean wind speed and the fitting coefficient of the vertical turbulence wind spectrum. In particular, the mean of the typhoon distribution is larger in comparison.

3.4. Pair copula for different wind climate

To assess variations in dependencies across different climate models, a copula function is formulated for the bivariate joint probability density function during typhoons and synoptic wind. The empirical Copula function between U and I_u under typhoon is estimated using Eq. (14), as shown in Fig. 9. The p -value of the symmetric hypothesis

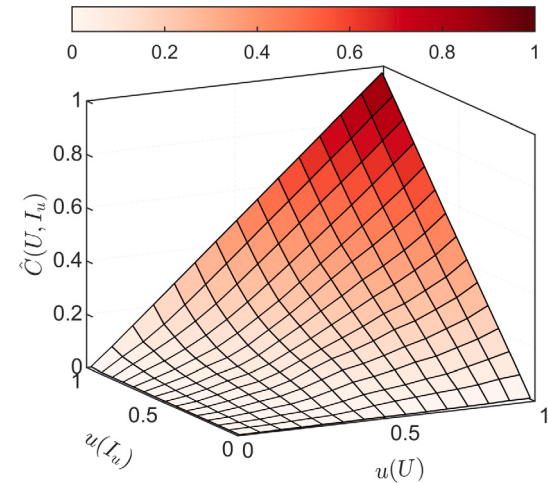


Fig. 9. Empirical Copula function between U and I_u .

(Eq. (15)) among them is 0.22, which indicates that the correlation can be described by a symmetric Copula function at the 0.05 significance level. The p -value of symmetry hypothesis test between other variables is shown in the Table 4. The hypothesis test proves that the dependence of turbulent wind parameters can be described by a symmetric copula function. Therefore, using the conventional Copula functions is appropriate.

The inference effect of underlying symmetric pair copulas in Table 1 was evaluated, and the joint PDF between mean wind speed and turbulence parameters is calculated according to Eq. (11). The most appropriate Copula function was selected according to the AIC and BIC criterion in Table 5. A similar comparative analysis is carried out for the synoptic wind between mean wind speed and turbulence parameters.

For the most appropriate copula, the fitting parameters are listed in Table 6, and the visualization is shown in the contour diagram in Fig. 10. The optimal copula family differs between typhoons and synoptic wind, indicating a significant disparity in the dependency patterns between mean wind speed and other variables of the wind environment under different wind conditions. Specifically, the synoptic wind exhibits a robust tail dependence in the low wind speed range, while the copula function for typhoons can be adequately described by the Gaussian copula. The copula functions between other binary variables can be referred to Tables B.1–B.5. in Appendix B.

3.5. Multi wind characteristics correlation modeling

The pair copula is employed to facilitate the establishment of multivariate dependencies. Following a selection criterion comparison of

Table 3
Statistical moments for marginal distribution.

Variables	Typhoon				Synoptic wind			
	Marginal name	μ_X	σ_X	Kstest-p	Marginal name	μ_X	σ_X	Kstest-p
U	Weibull	8.691	5.345	0.289	Weibull	5.867	3.798	0.738
α	Laplace	8.070	4.085		Gumbel	6.596	4.816	
I_u	Lognormal	0.201	0.146	0.086	Lognormal	0.166	0.110	0.105
I_w	Lognormal	0.101	0.078	0.639	Lognormal	0.082	0.053	0.435
L_u	Gamma	202.9	165.5	0.348	Gamma	167.5	134.8	0.207
L_w	Lognormal	63.41	61.59	0.467	Gamma	73.80	61.65	0.992
A_u	Gamma	2.704	1.105	0.943	Gamma	2.558	1.052	0.090
A_w	Weibull	3.520	1.188	0.060	Weibull	3.244	1.160	0.242

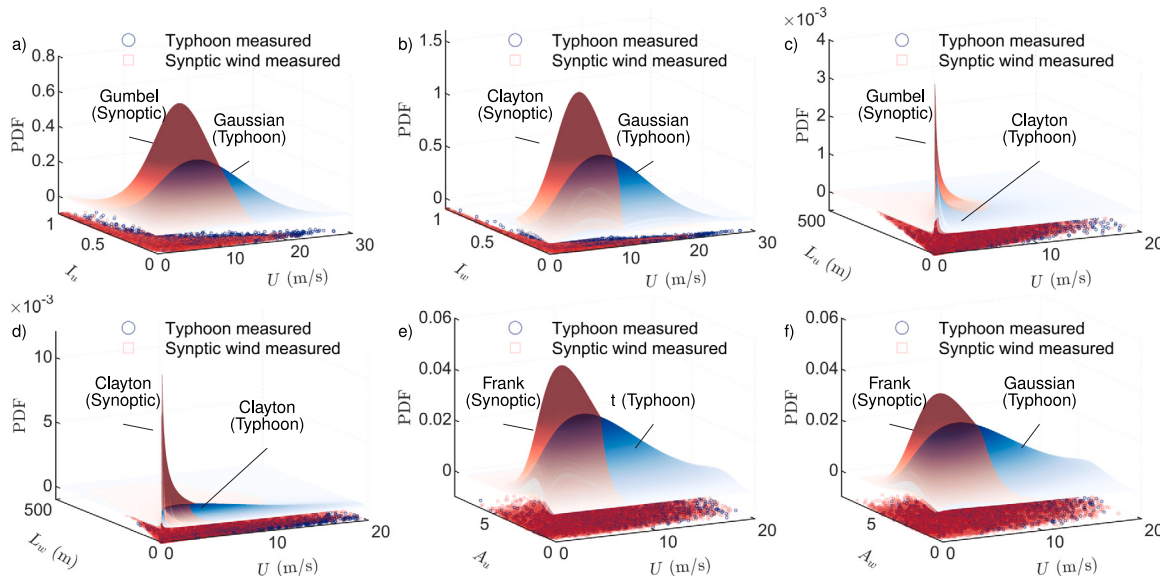


Fig. 10. Appropriate pair copula for bivariate between mean wind speed and turbulence characteristics: (a) U and I_u , (b) U and I_w , (c) U and L_u , (d) U and L_w , (e) U and A_u , (f) U and A_w .

Table 4
 p -value under typhoon: $p \leq 0.05$ means rejected H0.

	U	Iu	Iw	Lu	Lw	Au
Iu	0.22					
Iw	0.38	0.60				
Lu	0.92	0.10	0.60			
Lw	0.99	0.10	0.39	0.80		
Au	1.00	0.50	1.00	0.90	0.40	
Aw	0.70	0.80	0.90	0.20	0.20	1.00

various multivariate copula methods (given in Table 7), such as the Gaussian copula, C-vine, and D-vine, the fitted results indicate the selection of the Gaussian copula for constructing the multivariate correlation model. Additionally, the Gaussian copula facilitates a more convenient execution of isoprobabilistic transformation.

Given the relatively high dimensions of the input variables ($M = 8$), it becomes challenging to directly showcase the dependency disparity between the two wind environments. Following the derivation of the variable distribution with the Gaussian copula, the variables are segmented into two groups: along-wind turbulence parameters [U, I_u, L_u, A_u] and vertical turbulence parameters [I_w, L_w, A_w]. Segmentation is based on 5 m/s mean wind speed intervals: [0, 5] m/s, [5, 10] m/s, [10, 15] m/s, [15, 20] m/s, [20, 25] m/s, and [25, 30] m/s. The visualized results are presented in Figs. 11 to 14. The scattered points represent the sampling locations of the data, while the enveloping surfaces, distinguished by varying color shades, represent the joint PDF distribution constructed through the Gaussian copula function.

Fig. 11 illustrates the distribution of along-wind turbulent characteristics during typhoons across various wind speed ranges. Progressing from Fig. 11(a) to (f), the wind speed sequentially increases, and the visual transformation of the envelope surface evolves from being high and narrow to become flat and slender. This observation suggests lower turbulence intensity at higher wind speeds, accompanied by a gradual enlargement in the scale of the vortex and a discrete increase in energy distribution within the along-wind turbulence wind spectrum.

A comparison between Figs. 11 and 12 reveals distinctions in the distribution of the characteristics of turbulence along the wind during the typhoon and the synoptic wind. Specifically, when examining Figs. 11(a) and 12(a) (representing the comparison within the same wind speed interval), the envelope surface for the typhoon appears relatively larger. This suggests a comparatively higher turbulence intensity during typhoons, consequently leading to a more pronounced buffeting response at equivalent mean wind speeds. Furthermore, it should be noted that the synoptic wind turbulence integral scale exhibits a stronger correlation with the wind spectrum fitting parameters, indicating a more stable energy distribution within the synoptic wind turbulence spectrum.

Upon comparing Figs. 11 and 13, it becomes evident that the vertical envelope surface is comparatively smaller, signifying reduced vertical turbulence intensity and turbulence integral scale. Analytical observations made for the characteristics of the turbulence along the wind can be extended to the analysis of the vertical turbulence characteristics in Fig. 13, as well as Fig. 14.

In summary, the analysis of the transition from the marginal to joint distribution of typhoons and synoptic wind distinctly reveals a notable disparity between the two climates, characterized by the high and unstable turbulence energy for typhoons.

Table 5
Best fitted pair copula selection criteria under mean wind speed for typhoon.

U and I_u			U and I_w			U and L_u		
Name	AIC	BIC	Name	AIC	BIC	Name	AIC	BIC
Gaussian	-7161.6	-7153.6	Gaussian	-8479.3	-8471.3	Gaussian	-6750.7	-6742.6
Clayton	-6529.0	-6520.9	Clayton	-7090.7	-7082.7	Clayton	-7651.3	-7643.2
Gumbel	-6679.1	-6671.1	Gumbel	-7403.5	-7395.5	Gumbel	-7563.6	-7555.6
Frank	-6088.8	-6080.8	Frank	-6850.4	-6842.4	Frank	-5822.9	-5814.9
t	-7084.4	-7068.3	t	-8306.4	-8290.3	t	-6731.0	-6715.0
U and L_w			U and A_u			U and A_w		
Name	AIC	BIC	Name	AIC	BIC	Name	AIC	BIC
Gaussian	-2395.2	-2387.2	Gaussian	-926.8	-918.8	Gaussian	-1545.5	-1537.5
Clayton	-4365.4	-4357.4	Clayton	-764.7	-756.7	Clayton	-1096.6	-1088.6
Gumbel	-3830.8	-3822.8	Gumbel	-754.8	-746.8	Gumbel	-1153.6	-1145.6
Frank	-1723.0	-1714.9	Frank	-937.2	-929.2	Frank	-1477.3	-1469.3
t	-2500.6	-2484.6	t	-947.1	-931.0	t	-1451.4	-1435.3

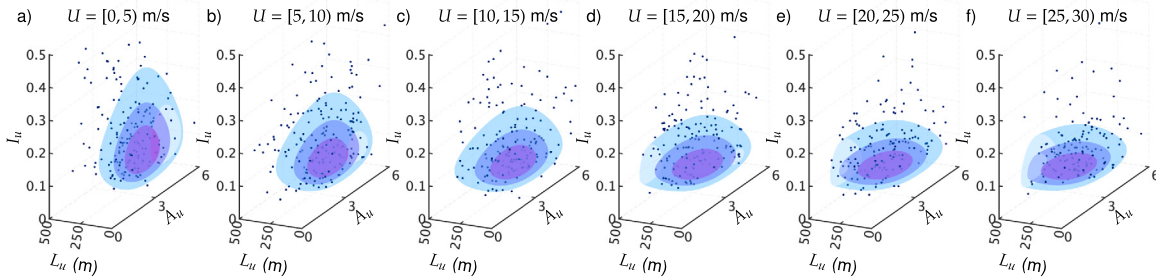


Fig. 11. Typhoon: Gaussian copula for along-wind turbulence characteristics correlation under different mean wind speed interval.

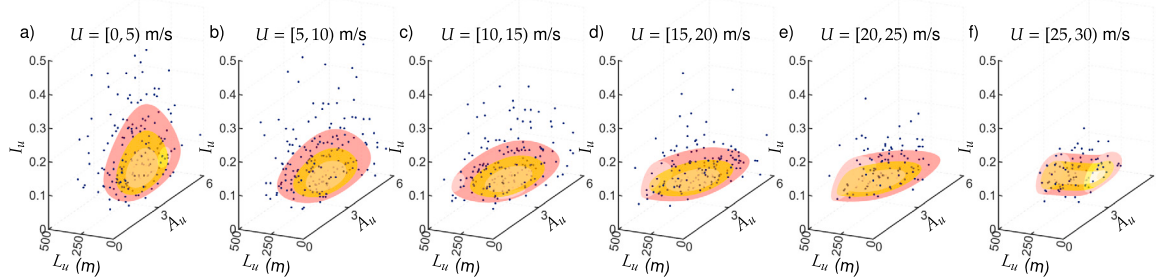


Fig. 12. Synoptic wind: Gaussian copula for along-wind turbulence characteristics correlation under different mean wind speed interval.

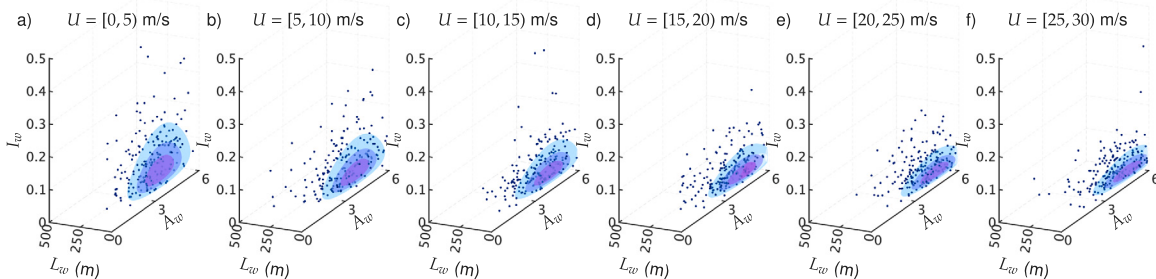


Fig. 13. Typhoon: Gaussian copula for vertical turbulence characteristics correlation under different mean wind speed interval.

3.6. Isoprobabilistic transformation: Nataf transformation

Following the establishment and examination of the distinctions between the two climates, it becomes evident that there are complex phenomena between turbulence variables that do not depend solely on the mean wind speed. To facilitate subsequent numerical simulations, it becomes imperative to transform the wind parameter distribution space into a standardized and independent distribution space.

Using Eqs. (20) to (23), a Nataf transformation is applied to the input space established by the Gaussian copula mentioned earlier. The results for typhoon and synoptic wind are depicted in Figs. 15 and 16. Designating 2000 sampling points in the original input parameter space, a standardized independent multidimensional Gaussian distribution is achieved through the Nataf transformation. It is important to highlight that the utilization of Gaussian copula in the Nataf transformation may lead to an underestimation of tail dependence probability,

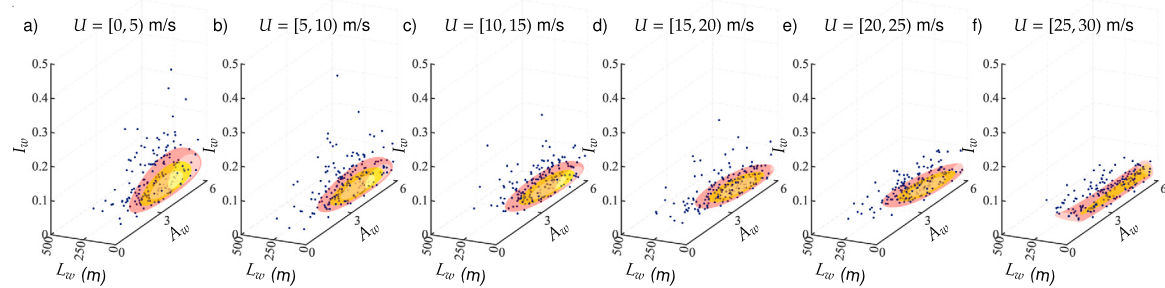


Fig. 14. Synoptic wind: Gaussian copula for vertical turbulence characteristics correlation under different mean wind speed interval.

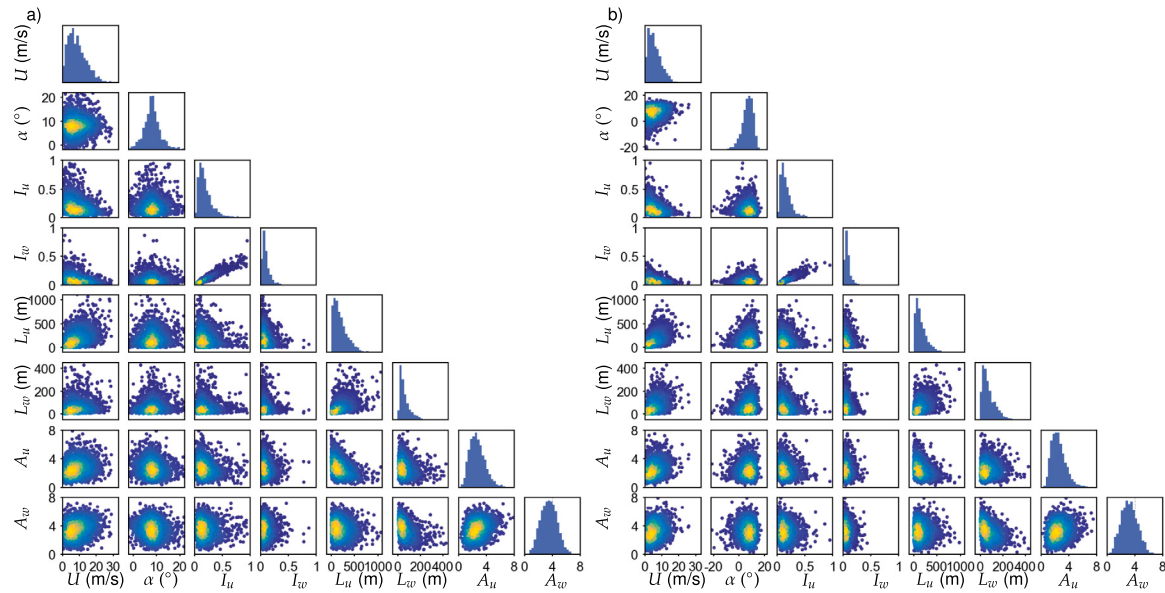


Fig. 15. Wind characteristic multiparameters based on Gaussian Copula: (a) typhoon, (b) synoptic wind.

Table 6

Pair copula parameters under mean wind speed.

Variables	Typhoon		Synoptic wind	
	Copula type	Parameters	Copula type	Parameters
I_u	Gaussian	$\theta = -0.520$	Gumbel	$\theta = 1.621$
I_w	Gaussian	$\theta = -0.558$	Clayton	$\theta = 0.912$
L_u	Clayton	$\theta = 0.904$	Gumbel	$\theta = 1.652$
L_w	Clayton	$\theta = 0.538$	Clayton	$\theta = 1.112$
A_u	t	$\theta = 0.202, v = 29.96$	Frank	$\theta = -1.612$
A_w	Gaussian	$\theta = 0.257$	Frank	$\theta = -1.432$

Table 7

Best fitted multivariable Copula (Gaussian and vine) selection criteria.

Typhoon		Synoptic wind			
Name	AIC	BIC	Name	AIC	BIC
Gaussian	-8920.65	-8765.38	Gaussian	-176 402.05	-176 163.37
C-vine	-6501.94	-6501.94	C-vine	-119 529.82	-119 529.82
D-vine	-7655.74	-7655.74	D-vine	-131 186.41	-131 186.41

as the tail dependence is not fully incorporated. Nevertheless, the current framework holds practical value. According to the preceding analysis, the parameter space can essentially be constructed using a Gaussian copula to establish a joint probability density function (PDF).

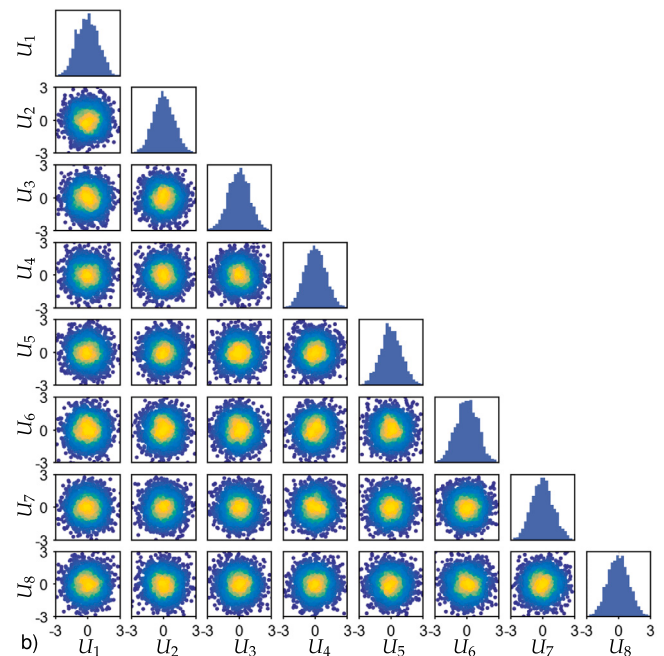


Fig. 16. Standard and independent Gaussian space.

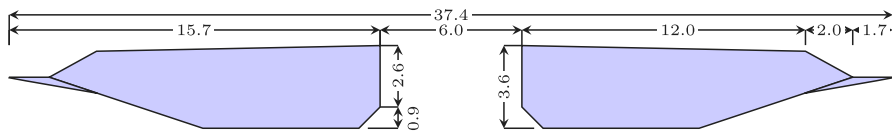


Fig. 17. Cross-section of Xihoumen Bridge (unit: m).

Table 8
Key parameters of Xihoumen Bridge.

Parameters	Values
Main span L (m)	1650
Side span L' (m)	578
Deck width B (m)	34 (eliminated wind skew)
Deck height H (m)	3.6
Mass per unit length M (kg/m)	27 511
Mass moment of inertial per unit length in longitudinal direction I (kg m)	4 002 800

4. Buffeting response calculation for multi-output based on surrogate model

4.1. Bridge information

The target bridge, the Xihoumen Bridge, is located in Zhoushan, Zhejiang Province in mainland China. The main bridge is a continuous steel-slotted box-girder suspension bridge, whose spans are 578 + 1650 + 485 m. The main girder comprises a separate steel box-girder section with a central 6.0-meter width slot, whose section width is 37.4 m and depth is 3.6 m (see Fig. 17).

A three-dimensional finite element model (FEM) of the bridge is formulated to extract its dynamic properties, encompassing natural frequency and mode shape. The key parameters of the FEM are shown in Table 8 [40].

The first six vibration modes are chosen for participation in the buffeting analysis (Fig. 18), which are 1st symmetric lateral bending (0.0482 Hz), 1st antisymmetric lateral bending (0.1074 Hz), 1st antisymmetric vertical bending (0.0790 Hz), 1st symmetric vertical bending (0.1002 Hz), 1st symmetric torsion (0.2335 Hz), and 1st antisymmetric torsion (0.2384 Hz).

Taking into account the impact of the angle of attack, Fig. 19 plots the three-component force coefficients measured in the Tongji University TJ-2 wind tunnel at AoAs ranging from -12° to $+12^\circ$. The coefficients of the drag force C_D and lift force are normalized to B and the coefficient of lifting moment C_M is normalized to B^2 . In Fig. 19, the positive direction of C_L is defined as the direction of the force that causes the main beam to move upward, and the directions of the other static forces are defined as in Fig. 5.

Fig. 20, the flutter derivatives H_i^* and A_i^* ($i = 1, 2, 3, 4$) are measured using the forced vibration method in the TJ-7 wind tunnel. Detailed measurements of the derivatives of flutter are made at different reduced wind speeds, including -3° , 0° and $+3^\circ$ for AoA, as well as partially reduced wind speeds of -3.5° , 0.5° , 4° and 4.5° . All flutter derivatives from -3° to $+15^\circ$ are obtained by interpolation fitting. To mitigate potential inaccuracies resulting from extrapolation, the extrapolation format is set to nearest. P_1^* to P_6^* , H_5^* , H_6^* , A_5^* , A_6^* are based on the quasi-steady theory [65], and the angle of attack effect of lateral dependent derivative is not considered.

In the input variables, only the autospectral density for turbulence is used. The normalized cross-spectral density ($C_a(\kappa)$ in Eq. (37)) in the conventional form as [66]:

$$C_a = \exp\left(-\frac{c\Delta x}{l}\right) \quad (43)$$

where the $c = 7\kappa l/2\pi B$. The admittance function $\chi(\kappa)$ uses the Sears function:

$$\chi = \frac{1}{1 + \pi(2\pi/\kappa)} \quad (44)$$

4.2. Surrogate modeling based on frequency domain calculation of bridge buffeting

The frequency domain for multi-mode buffeting involves solving the response spectrum at each frequency point using modal coordinates. However, due to the impact of modal coupling, the double integral must be computed multiple times, which requires significant computational resources. As a result, direct sampling of the input variables of the wind environment through MC simulation is impractical. Instead, a PCE surrogate model is employed. This model selects orthogonal polynomials consistent with the edges of the variable distribution, and a limited set of sampling points is chosen to calculate the frequency domain, constructing an efficient surrogate model. This approach facilitates the probabilistic propagation of the input dependencies of the wind environment onto the response.

Within the surrogate model, the output variables contain vertical, lateral, and torsional responses at the 1/2 span and 1/4 span, and multi-outputs are considered. The LAR method is used to obtain the polynomial coefficients y_p . Fig. 21 shows the two types of regression error function, namely the LOO error and the relative training error (defined in Eq. (41)), change with the number of sample points for multi-output buffeting response under typhoon climate. For each fixed sample point, the degree of the polynomial is set from 2 to 16, and the one with the smallest LOO error is selected as the best optimal PCE model under this sampling number. One advantage of the sparse PCE approach is that it can approximate the original multimode frequency domain buffeting computation method by choosing a small number of sample points. For typhoon configuration, the computational model can be well approximated by PCE when selecting 500 sample points, and the degree of polynomial is 7.

To enhance the evaluation of the predictive capabilities of the established surrogate model and verify the validation of PCE in high dimensional variables, 200 new sample points from the standard and independent 8-dimensional normal distribution space are extracted. Using an inverse Nataf transformation, these samples are transformed into the sample space corresponding to the wind environment of the typhoon. Subsequently, the multimode frequency domain buffeting method and the PCE surrogate model were utilized to compute the vertical, lateral and torsional responses of the 1/2 span and 1/4 span, respectively. The result is given in Fig. 22. The consistency R^2 reaches 0.95 regardless of the 1/2 or 1/4 span. In other words, the surrogate model has superior generalization capacity and the coefficient is valued according to the LAR technique. The surrogate model can be used to conduct a large number of subsequent MC simulations to explore the distribution and dependence of responses in the two climates.

The above verification only proves that the surrogate model can fit the original computational model well. Whether the calculated results are consistent with the on-site monitoring data still needs further verification. To verify the difference between the surrogate model based on the multi-mode buffeting frequency domain theory and the measured displacement response by the on-site monitoring acceleration data, the measured acceleration spectrum is first transformed into a displacement spectrum, whose integral of the frequency axis among [0.01, 1] Hz is the RMS squared value of wind-induced buffeting displacement to avoid [67]. Consider the response in midspan, the comparison between calculated results of PCE surrogate model and measured displacement response is shown in Fig. 23. The histogram shows that the distribution of the numerical calculation results is basically consistent with the

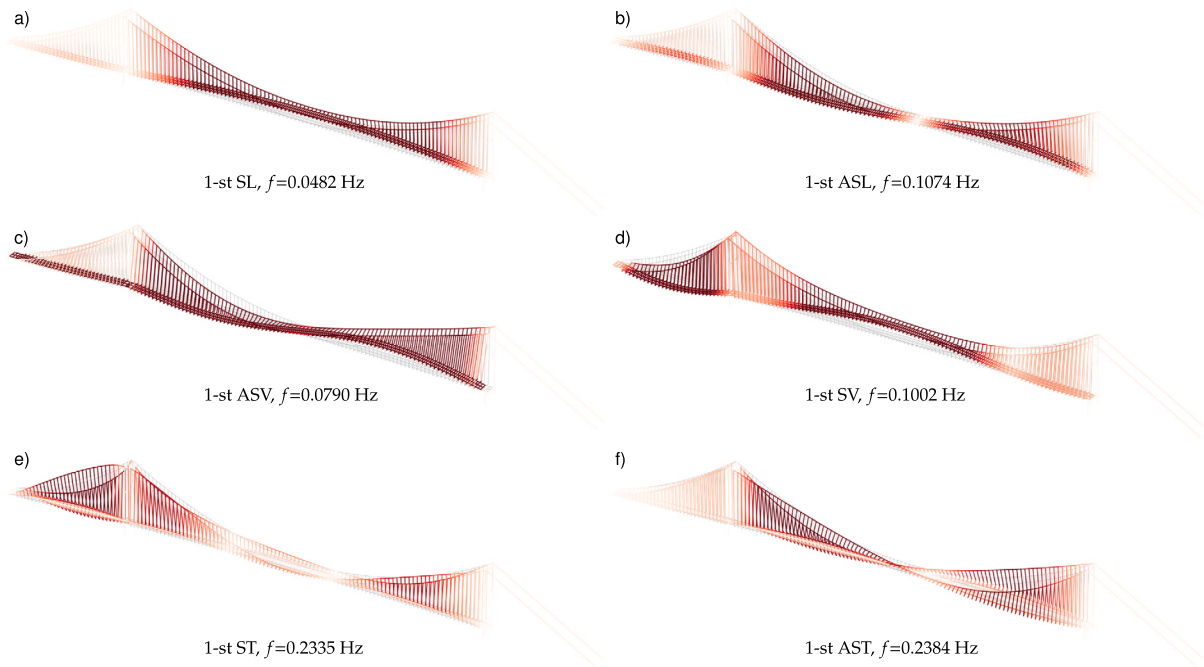


Fig. 18. Main mode shape of Xihoumen Bridge: (a) 1st SL, (b) 1st ASL, (c) 1st ASV, (d) 1st SV, (e) 1st ST, (f) 1st AST.

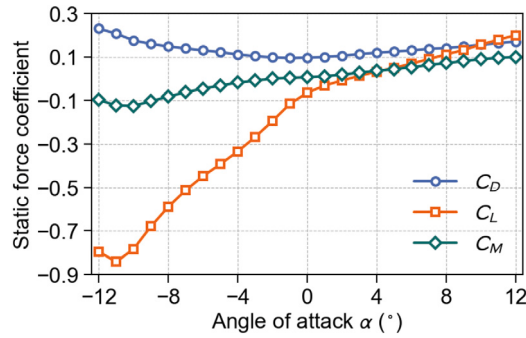


Fig. 19. Static force coefficients with angle of attack.

actual observed values for vertical and torsional displacement, but the lateral displacement is overestimated. As mentioned above, the derivatives related to lateral bending adopt the result of quasi-steady theory when $\alpha = 0^\circ$, which may have a big difference between quasi-steady flutter derivatives and real flutter derivatives for a central slotted section like Xihoumen Bridge.

To summarize, this section develops a frequency-domain multi-mode buffeting response surrogate model combined Nataf transformation and Polynomial Chaos Expansion. The accuracy of the surrogate model is validated through comparison with both the original calculation model and on-site monitoring data.

4.3. Probabilistic response under different DoFs

A total of 10 000 Monte Carlo simulations are performed on the surrogate model, simulating the buffeting response under typhoons and synoptic wind. The results obtained include the vertical, lateral and torsional root mean square (RMS) responses in the middle of the span and quartile points of the main beam. Fig. 24 shows the marginal

Table 9
Fitting parameter of Lognormal distribution for buffeting response.

Variables	Typhoon			Synoptic wind		
	ζ	μ	λ	ζ	μ	λ
$\sigma_{hh,1/2}$	1.0796	0.0748	-0.1830	0.9571	0.0671	-0.7771
$\sigma_{pp,1/2}$	1.1147	-0.0366	1.8100	0.9837	0.0894	1.0447
$\sigma_{aa,1/2}$	1.0474	0.0009	-5.3561	0.9865	0.0010	-6.0466
$\sigma_{hh,1/4}$	1.0911	0.0933	0.3730	0.9448	0.0787	-0.2001
$\sigma_{pp,1/4}$	1.1184	-0.0124	1.3353	0.9993	0.0756	0.5542
$\sigma_{aa,1/4}$	1.0534	0.0008	-5.4653	0.9636	0.0008	-6.1304

distribution under different climate, and the Lognormal distribution with location parameter is used to fit it, which is defined as:

$$f(x; \mu, \lambda, \zeta) = \frac{1}{(x - \mu)\zeta\sqrt{2\pi}} \exp\left(-\frac{(\ln(x - \mu) - \lambda)^2}{2\zeta^2}\right) \quad (45)$$

where μ is location parameter and others can refer to Table A.1. The marginal distribution pass the K-S test and the fitting parameter is given in Table 9. It can be found that for the three degrees of freedom, the response distribution under typhoon is higher than that under synoptic wind, but the key wind parameters that really affect the structural response still need to be discussed later.

Figs. 25 show the output in the middle of the span under typhoon and synoptic wind, and a quadratic polynomial was employed to fit their most probable values (MPV) with average wind speed. The red surfaces in subfigure (a) to (c) represent the relative probability of the displacement response occurring in the typhoon input parameters, and blue one represent that in the synoptic wind input parameters. In comparison, the response under typhoons tends to be more discrete at the similar wind speed. This suggests, on the one hand, that wind-induced responses under typhoons are intricate and cannot be adequately captured by a single mean wind speed. Instead, it should be considered within the context of multiparameters of the wind environment. Although they are relatively smaller in magnitude, the responses during typhoons are notable for their complexity.

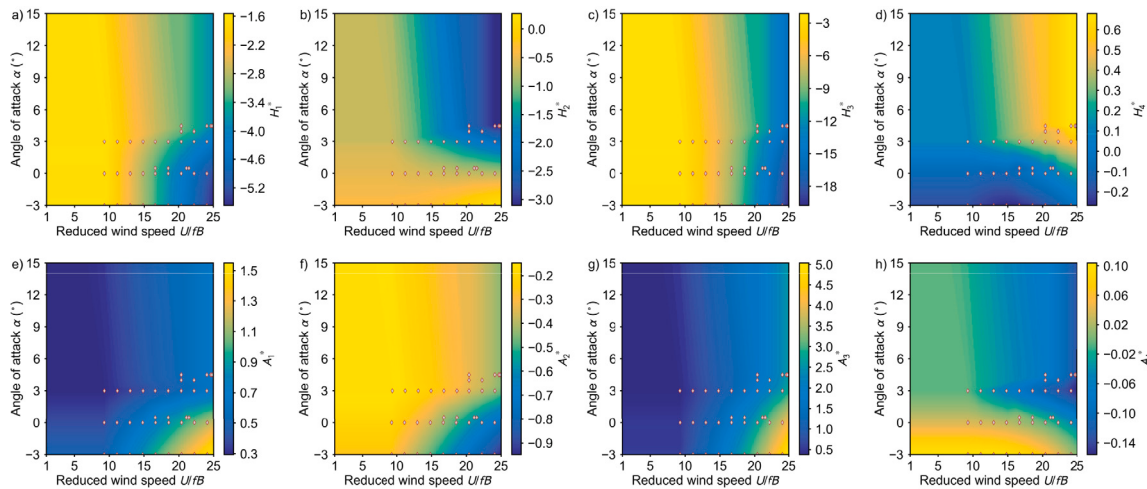


Fig. 20. Flutter derivatives with reduced wind speed and angle of attack.

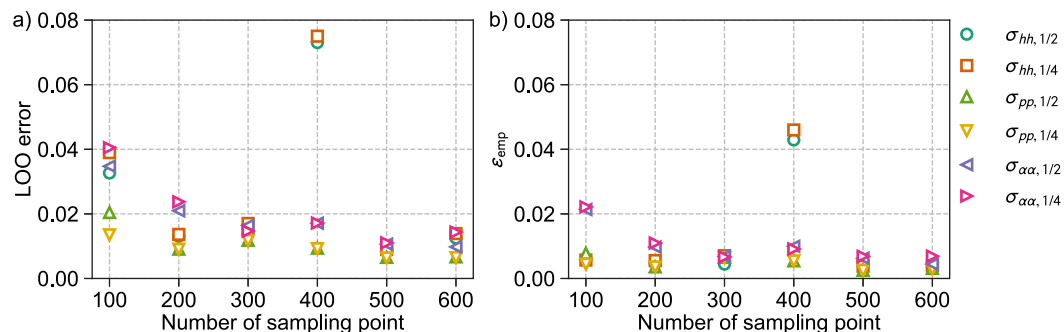


Fig. 21. PCE error changed with the number of sample points under typhoon: (a) LOO error, (b) relative training error.

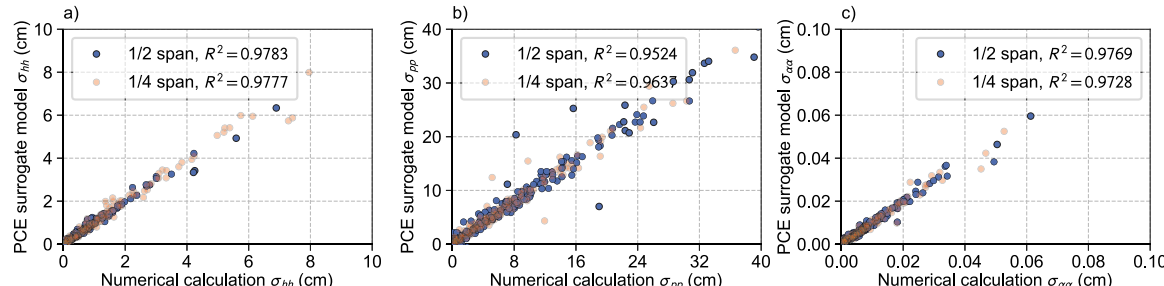


Fig. 22. PCE surrogate model verification when number of sample = 200, degree = 7 under typhoon: (a) vertical displacement RMS, (b) lateral displacement RMS, (c) torsional displacement RMS.

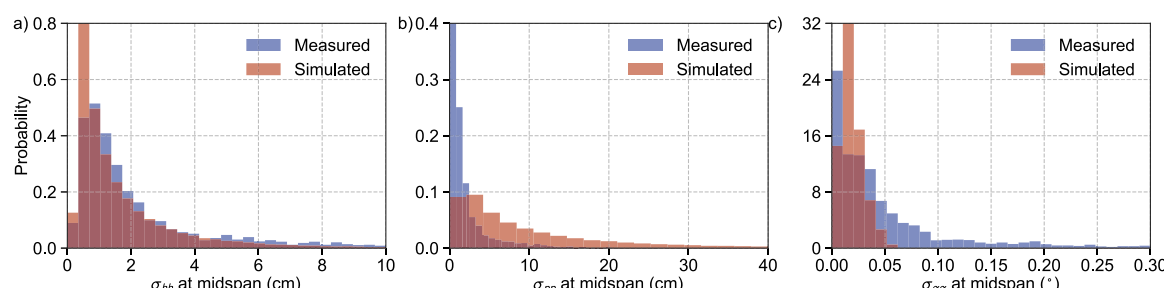


Fig. 23. Comparison between measured and simulated displacement: (a) vertical displacement RMS, (b) lateral displacement RMS, (c) torsional displacement RMS.

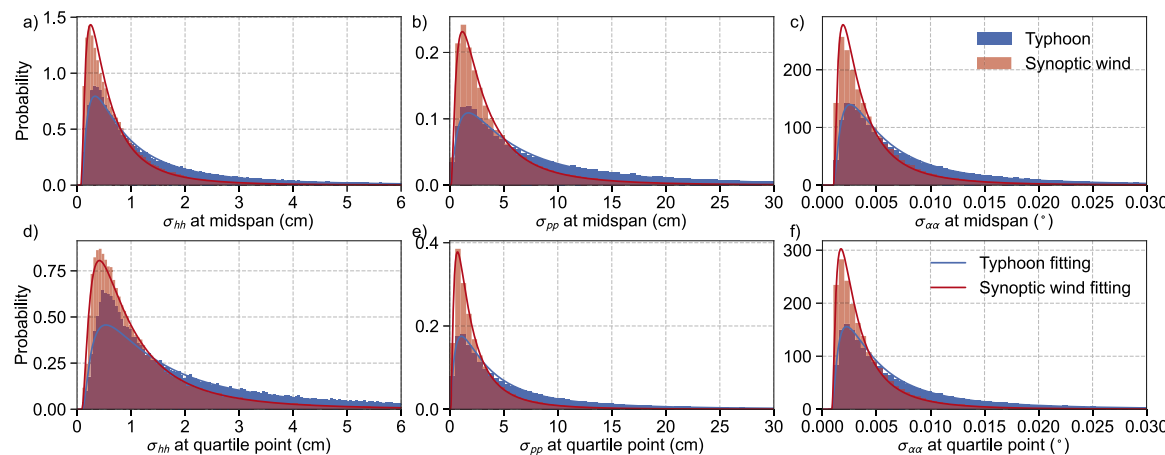


Fig. 24. Marginal distribution for displacement under typhoon and synoptic wind: (a)~(c) vertical, lateral and torsional displacement RMS at midspan, (d)~(f) vertical, lateral and torsional displacement RMS at quartile point.

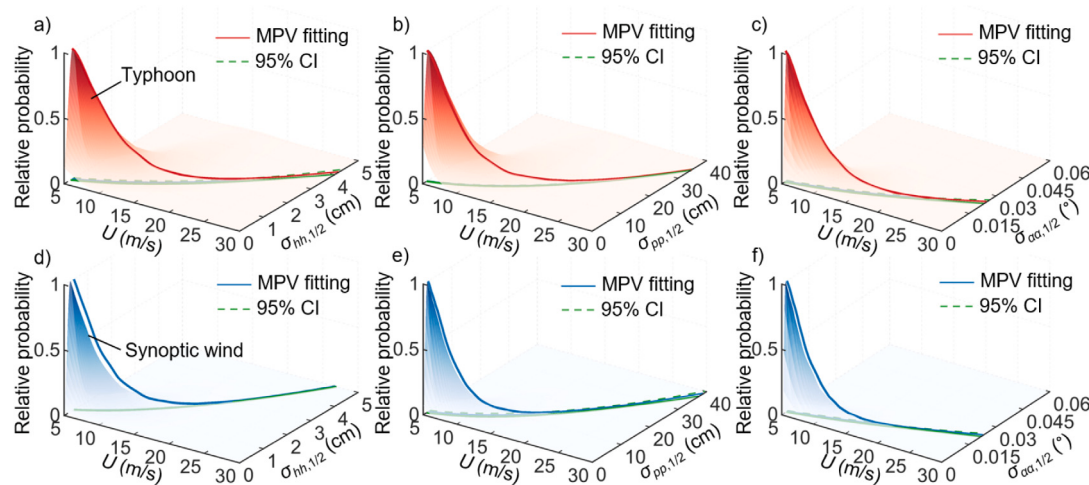


Fig. 25. PCE estimate result of midspan displacement with average wind speed: (a)~(c) vertical, lateral and torsional displacement for typhoon, (d)~(f) vertical, lateral and torsional displacement for synoptic wind.

The wind environment parameters that affect the structural response may be complex, but the established surrogate model is particularly suitable for exploring the response under different wind environment values due to its high computational efficiency. In order to directly show the influence of U and I_u on response, and the joint distribution established by the pair Copula function (Fig. 10) was used to calculate their response under different environmental contour. The mean value of other turbulence parameters was taken in Table 3, and the results were shown in Fig. 26. The phenomena clearly demonstrate that while average wind speed is a key factor influencing the response, along-wind turbulence intensity must also be considered in the analysis. It cannot be treated as a fixed value determined solely by surface roughness. Instead, its correlation with average wind speed should be thoroughly analyzed. Since this study provides statistical results from specific bridge sites under various wind conditions, it is not feasible to recommend a universal value applicable to all surface types. However, the correlation model outlined in the paper remains a valuable addition to existing standards and guidelines. The influence of other binary or higher-dimensional input parameters on the wind-induced response is limited by the length of the article and will not be elaborated upon here.

However, another interesting issue, which has not been mentioned by the existing research, is the dependency between the responses

under different degrees of freedom and different cross sections that can be obtained according to the input space and the response surrogate model. Since the involvement of multiple modes makes it challenging to ascertain whether the response strictly adheres to linearity concerning multi-output through analytical expressions, the dependency of the response is established based on the results of 10 000 calculations.

As expected in Fig. 27, substantial correlation is observed. The responses at different cross sections with the same degree of freedom show strong linear correlation. In contrast, responses with different degrees of freedom show a weak tail dependence, and the joint distribution of binary variables can be described by Gumbel copula. The Gaussian and vine structures are compared respectively for multi-output correlation modeling, and it is found that the AIC and BIC values of D-vine are the smallest. The results in Fig. 27 also emphasize here that the response is greater under typhoons.

In conclusion, a surrogate model is employed to simulate the dependence of multi-output responses, starting from the established multivariable wind environment parameter space and theoretical formulas. The observations reveal intricate and nonlinear correlations between responses across various cross sections and degrees of freedom, and there are also large differences in the structural effects caused by typhoons and synoptic wind.

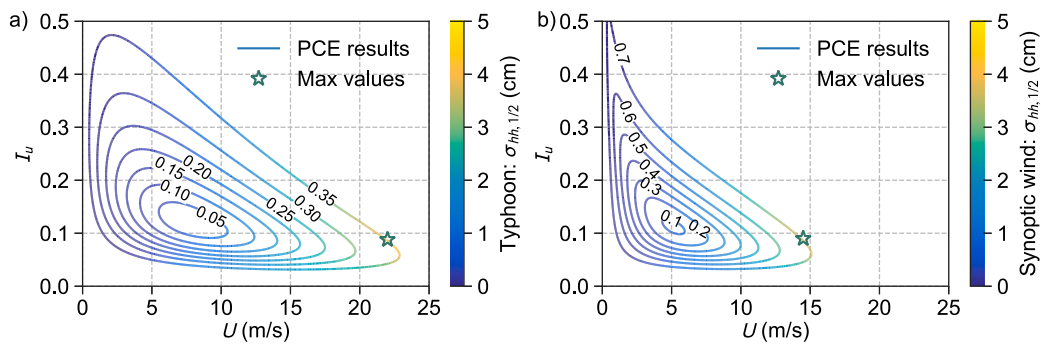


Fig. 26. Vertical buffeting response at midspan under different probability between U and I_u : (a) typhoon, (b) synoptic wind.

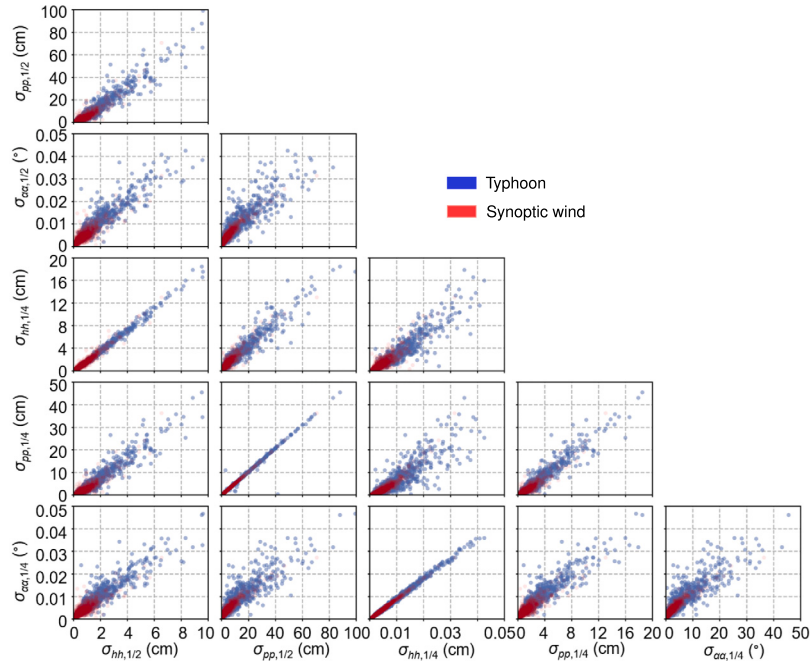


Fig. 27. Correlation of multiple output responses for 1000 times simulation.

5. Conclusions

Drawing on 12 years of wind environment data obtained from the health monitoring of a long-span suspension bridge, this paper reveals the dependency distinctions in wind environmental parameters between typhoons and synoptic conditions and establishes a multivariable model. Furthermore, using a surrogate model coupled with isoprobabilistic transformation, the impact of variations in wind environment input parameters on structural effects is investigated, leading to the following conclusions.

- The turbulence parameters under typhoon conditions can be characterized by a Gaussian copula, highlighting increased turbulence intensity and a more dispersed distribution of wind spectrum energy. Notably, at higher wind speeds, there is a stronger correlation between the turbulence length scale and the wind spectrum fitting parameters. This suggests that, at high wind speeds, the wind spectrum is more significantly influenced by larger eddies.
- The turbulence parameters of typhoons tend to result in higher wind-induced responses. Evaluating these responses during typhoons requires more than just the mean wind speed index; it necessitates a comprehensive assessment of other turbulence parameters. Moreover, the responses across different degrees of freedom exhibit nonlinear dependencies.

- The Kaimal-form wind spectrum can be fitted to the along-wind and vertical turbulence spectra, with a relatively better fit for synoptic wind conditions.

CRediT authorship contribution statement

Peng Liu: Writing – original draft, Visualization, Validation, Methodology, Investigation, Formal analysis, Conceptualization. **Wei Cui:** Writing – review & editing, Supervision, Funding acquisition, Conceptualization. **Lin Zhao:** Supervision, Funding acquisition.

Declaration of competing interest

The authors declare that they have no known competing financial interests or personal relationships that could have appeared to influence the work reported in this paper.

Acknowledgments

The authors gratefully acknowledge the support of National Key Research and Development Program of China (2021YFF0502200, 2022YFC3005302) and National Natural Science Foundation of China (52478552). Any opinions, findings and conclusions are those of the authors and do not necessarily reflect the reviews of the above agencies.

Table A.1

Marginal distribution used in this study: μ_X and σ_X the mean and variance of measured X , respectively; $\mu, \sigma, \lambda, \zeta, \beta, \alpha, k, b$ is the parameters to be estimated for marginal distribution; $\Gamma(x)$ is the Gamma function; $\lambda_e \approx 0.5772$ is the Euler constant.

Name	PDF ($f_X(x)$)	CDF ($F_X(x)$)	Parameters and moments
Gaussian	$\frac{1}{\sqrt{2\pi}\sigma} e^{-\frac{(x-\mu)^2}{2\sigma^2}}$	$\int_{-\infty}^{\frac{x-\mu}{\sigma}} \frac{e^{-t^2/2}}{\sqrt{2\pi}} dt$	$\mu_X = \mu$ $\sigma_X = \sigma$
Lognormal	$\frac{1}{\sqrt{2\pi}\zeta x} e^{-\frac{(\ln x - \lambda)^2}{2\zeta^2}}$	$\int_{-\infty}^{\frac{\ln x - \lambda}{\zeta}} \frac{e^{-t^2/2}}{\sqrt{2\pi}} dt$	$\mu_X = e^{\lambda + \zeta^2/2}$ $\sigma_X = e^{\lambda + \zeta^2/2} \sqrt{e^{\zeta^2} - 1}$
Gumbel-min	$\frac{1}{\beta} e^{-\frac{x-\mu}{\beta}} e^{-e^{-\frac{x-\mu}{\beta}}}$	$1 - e^{-e^{-\frac{x-\mu}{\beta}}}$	$\mu_X = \mu - \beta\gamma_e$ $\sigma_X = \frac{\pi\beta}{\sqrt{6}}$
Weibull	$\begin{cases} \frac{\beta}{\alpha} \left(\frac{x}{\alpha} \right)^{\beta-1} e^{-(x/\alpha)^\beta}, & x \geq 0 \\ 0, & x < 0 \end{cases}$	$\begin{cases} 1 - e^{-(x/\alpha)^\beta}, & x \geq 0 \\ 0, & x < 0 \end{cases}$	$\mu_X = \alpha \Gamma(1 + 1/\beta)$ $\sigma_X = \alpha \sqrt{\Gamma(1 + \epsilon/\beta) - \Gamma(1 + 1/\beta)^2}$
Gamma	$\frac{\lambda^k}{\Gamma(k)} X^{k-1} e^{-\lambda x}$	$\frac{\gamma(k, \lambda x)}{\Gamma(k)}$	$\mu_X = \frac{k}{\lambda}$ $\sigma_X = \frac{\sqrt{k}}{\lambda}$
Laplace	$\frac{1}{2b} e^{-\frac{ x-\mu }{b}}$	$\begin{cases} \frac{1}{2} e^{-\frac{x-\mu}{b}}, & x < \mu \\ 1 - \frac{1}{2} e^{-\frac{x-\mu}{b}}, & x \leq \mu \end{cases}$	$\mu_X = \mu$ $\sigma_X = b\sqrt{2}$

Table B.1

Pair copula parameters under along-wind turbulence intensity.

Variables	Typhoon		Synoptic wind	
	Copula type	Parameters	Copula type	Parameters
I_w	t	$\theta = 0.940, v = 10.218$	t	$\theta = 0.891, v = 10.637$
L_u	Clayton	$\theta = 0.286$	Clayton	$\theta = 0.338$
L_w	Clayton	$\theta = 0.277$	Gumbel	$\theta = 1.294$
A_u	Gaussian	$\theta = -0.131$	Frank	$\theta = -1.450$
A_w	Clayton	$\theta = 0.052$	Clayton	$\theta = 0.079$

Table B.2

Pair copula parameters under vertical turbulence intensity.

Variables	Typhoon		Synoptic wind	
	Copula type	Parameters	Copula type	Parameters
L_u	Gaussian	$\theta = -0.423$	Gaussian	$\theta = -0.470$
L_w	Clayton	$\theta = 0.314$	Clayton	$\theta = 0.391$
A_u	Independent		Clayton	$\theta = 0.0421$
A_w	Independent		Frank	$\theta = -0.480$

Table B.3

Pair copula parameters under along-wind turbulence length scale.

Variables	Typhoon		Synoptic wind	
	Copula type	Parameters	Copula type	Parameters
L_w	t	$\theta = 0.500, v = 15.453$	Clayton	$\theta = 1.0814$
A_u	Frank	$\theta = -3.049$	Gaussian	$\theta = -0.350$
A_w	Clayton	$\theta = 0.116$	t	$\theta = 0.0122, v = 29.977$

Table B.4

Pair copula parameters under vertical turbulence length scale.

Variables	Typhoon		Synoptic wind	
	Copula type	Parameters	Copula type	Parameters
A_u	Clayton	$\theta = 0.195$	Clayton	$\theta = 0.078$
A_w	Clayton	$\theta = 0.782$	Gaussian	$\theta = -0.368$

Appendix A. Marginal distribution used in this study

See Table A.1.

Appendix B. Pair copula for different wind climate

See Tables B.1–B.5.

Table B.5

Pair copula parameters under vertical turbulence length scale.

Variables	Typhoon		Synoptic wind	
	Copula type	Parameters	Copula type	Parameters
A_w	Gumbel	$\theta = 1.204$	Gumbel	$\theta = 1.159$

References

- [1] Holmes JD, Paton C, Kerwin R. Wind loading of structures. CRC Press; 2007.
- [2] Eryilmaz S, Bulanik İ, Devrim Y. Reliability based modeling of hybrid solar/wind power system for long term performance assessment. Reliab Eng Syst Saf 2021;209:107478.
- [3] Cantwell BJ. Organized motion in turbulent flow. Annu Rev Fluid Mech 1981;13(1):457–515.
- [4] American Society of Civil Engineers. Minimum design loads for buildings and other structures. Reston, VA, U.S.A.: American Society of Civil Engineers; 2017.
- [5] Fujino Y, Kimura K, Tanaka H. Wind resistant design of bridges in Japan: Developments and practices. Springer Science & Business Media; 2012.
- [6] Huang Z, Rosowsky DV, Sparks PR. Long-term hurricane risk assessment and expected damage to residential structures. Reliab Eng Syst Saf 2001;74(3):239–49.
- [7] Emanuel K. Increasing destructiveness of tropical cyclones over the past 30 years. Nature 2005;436(7051):686–8.
- [8] Chu X, Cui W, Zhao L, Cao S, Ge Y. Probabilistic flutter analysis of a long-span bridge in typhoon-prone regions considering climate change and structural deterioration. J Wind Eng Ind Aerodyn 2021;215:104701.
- [9] Shen Z, Wei K. Stochastic model of tropical cyclones along China coast including the effects of spatial heterogeneity and ocean feedback. Reliab Eng Syst Saf 2021;216:108000.
- [10] Vickery P, Skerlj P, Twisdale L. Simulation of hurricane risk in the US using empirical track model. J Struct Eng 2000;126(10):1222–37.
- [11] Krämer WR, Marshall RD. Gust factors applied to hurricane winds. Bull Am Meteorol Soc 1992;73(5):613–8.
- [12] Cao S, Tamura Y, Kikuchi N, Saito M, Nakayama I, Matsuzaki Y. A case study of gust factor of a strong typhoon. J Wind Eng Ind Aerodyn 2015;138:52–60.
- [13] Zhao L, Cui W, Ge Y. Measurement, modeling and simulation of wind turbulence in typhoon outer region. J Wind Eng Ind Aerodyn 2019;195:104021.
- [14] Song L-L, Mao H-q, Tang H-y, Liu A. Observation and analysis of Guangdong coastal gales in the near-surface layer. J Trop Meteorol 2004;20(6):731–6.
- [15] Shu Z, Li Q, He Y, Chan P. Vertical wind profiles for typhoon, monsoon and thunderstorm winds. J Wind Eng Ind Aerodyn 2017;168:190–9.
- [16] Wang H, Li A, Niu J, Zong Z, Li J. Long-term monitoring of wind characteristics at Sutong bridge site. J Wind Eng Ind Aerodyn 2013;115:39–47.
- [17] Fang G, Zhao L, Cao S, Ge Y, Li K. Gust characteristics of near-ground typhoon winds. J Wind Eng Ind Aerodyn 2019;188:323–37.
- [18] Yi G, Pan J, Zhao L, Song L, Fang G, Cui W, Ge Y. Profiles of mean wind and turbulence intensity during strong typhoon landfall. J Wind Eng Ind Aerodyn 2022;228:105106.
- [19] Li L, Kareem A, Hunt J, Xiao Y, Zhou C, Song L. Turbulence spectra for boundary-layer winds in tropical cyclones: A conceptual framework and field measurements at coastlines. Bound-Layer Meteorol 2015;154(2):243–63.

- [20] Fenerci A, Øiseth O. Site-specific data-driven probabilistic wind field modeling for the wind-induced response prediction of cable-supported bridges. *J Wind Eng Ind Aerodyn* 2018;181:161–79.
- [21] Liu Z, Fang G, Hu X, Xu K, Zhao L, Ge Y. Stochastic power spectra models for typhoon and non-typhoon winds: A data-driven algorithm. *J Wind Eng Ind Aerodyn* 2022;231:105214.
- [22] Nelsen RB. An introduction to copulas. Springer; 2006.
- [23] Fang G, Pan R, Hong Y. Copula-based reliability analysis of degrading systems with dependent failures. *Reliab Eng Syst Saf* 2020;193:106618.
- [24] Li H-N, Zheng X-W, Li C. Copula-based joint distribution analysis of wind speed and direction. *J Eng Mech* 2019;145(5):04019024.
- [25] Wang Z-w, Zhang W-m, Tian G-m, Liu Z. Joint values determination of wind and temperature actions on long-span bridges: Copula-based analysis using long-term meteorological data. *Eng Struct* 2020;219:110866.
- [26] Zhang J, Zhang M, Jiang X, Wu L, Qin J, Li Y. Pair-copula-based trivariate joint probability model of wind speed, wind direction and angle of attack. *J Wind Eng Ind Aerodyn* 2022;225:105010.
- [27] Hu X, Fang G, Yang J, Zhao L, Ge Y. Simplified models for uncertainty quantification of extreme events using Monte Carlo technique. *Reliab Eng Syst Saf* 2023;230:108935.
- [28] Winterstein SR, Ude TC, Cornell CA, Bjerager P, Haver S. Environmental parameters for extreme response: Inverse FORM with omission factors. In: Proceedings of the ICOSSAR-93, Innsbruck, Austria. 1993, p. 551–7.
- [29] Lystad TM, Fenerci A, Øiseth O. Buffeting response of long-span bridges considering uncertain turbulence parameters using the environmental contour method. *Eng Struct* 2020;213:110575.
- [30] Lystad TM, Fenerci A, Øiseth O. Long-term extreme buffeting response of cable-supported bridges with uncertain turbulence parameters. *Eng Struct* 2021;236:112126.
- [31] Lystad TM, Fenerci A, Øiseth O. Full long-term extreme buffeting response calculations using sequential Gaussian process surrogate modeling. *Eng Struct* 2023;292:116495.
- [32] Hu X, Fang G, Ge Y. Uncertainty propagation of flutter derivatives and structural damping in buffeting fragility analysis of long-span bridges using surrogate models. *Struct Saf* 2024;106:102410.
- [33] Castellon DF, Fenerci A, Petersen ØW, Øiseth O. Full long-term buffeting analysis of suspension bridges using Gaussian process surrogate modelling and importance sampling Monte Carlo simulations. *Reliab Eng Syst Saf* 2023;235:109211.
- [34] Allahvirdizadeh R, Andersson A, Karoumi R. Applicability of meta-model assisted reliability assessment for dynamic problems: a comparison between regression-based methods. In: 14th international conference on applications of statistics and probability in civil engineering. ICASPI4, 2023.
- [35] Laima S, Feng H, Li H, Jin Y, Han F, Xu W. A buffeting-net for buffeting response prediction of full-scale bridges. *Eng Struct* 2023;275:115289.
- [36] Yao W, Zheng X, Zhang J, Wang N, Tang G. Deep adaptive arbitrary polynomial chaos expansion: A mini-data-driven semi-supervised method for uncertainty quantification. *Reliab Eng Syst Saf* 2023;229:108813.
- [37] Zhang J, Gong W, Yue X, Shi M, Chen L. Efficient reliability analysis using prediction-oriented active sparse polynomial chaos expansion. *Reliab Eng Syst Saf* 2022;228:108749.
- [38] Palan PS, Zuhal LR, Shimoyama K. Enhancing the explainability of regression-based polynomial chaos expansion by Shapley additive explanations. *Reliab Eng Syst Saf* 2023;232:109045.
- [39] Liu W, Chen Ej, Yao E, Wang Y, Chen Y. Reliability analysis of face stability for tunnel excavation in a dependent system. *Reliab Eng Syst Saf* 2021;206:107306.
- [40] Liu Z, Fang G, Zhao L, Ge Y. Uncertainty propagation of turbulence parameters for typhoon and non-typhoon winds in buffeting analysis of long-span bridges. *Eng Struct* 2023;291:116491.
- [41] Ciampoli M, Petrini F, Augusti G. Performance-based wind engineering: Towards a general procedure. *Struct Saf* 2011;33(6):367–78.
- [42] Kareem A, Tamura Y. Advanced structural wind engineering, vol. 482, Springer; 2013.
- [43] Li C, Pan H, Tian L, Bi W. Lifetime multi-hazard fragility analysis of transmission towers under earthquake and wind considering wind-induced fatigue effect. *Struct Saf* 2022;99:102266.
- [44] Der Kiureghian A, Liu P-L. Structural reliability under incomplete probability information. *J Eng Mech* 1986;112(1):85–104.
- [45] Buckingham E. Model experiments and the forms of empirical equations. *J Fluids Eng* 1915;37:263–92.
- [46] Fenerci A, Øiseth O. Strong wind characteristics and dynamic response of a long-span suspension bridge during a storm. *J Wind Eng Ind Aerodyn* 2018;172:116–38.
- [47] Welch P. The use of fast Fourier transform for the estimation of power spectra: a method based on time averaging over short, modified periodograms. *IEEE Trans Audio Electroacoust* 1967;15(2):70–3.
- [48] Huang Y, Zhang B, Pang H, Wang B, Lee KY, Xie J, Jin Y. Spatio-temporal wind speed prediction based on Clayton Copula function with deep learning fusion. *Renew Energy* 2022;192:526–36.
- [49] Yang P-H, Yu Y, Gu F, Qu M-J, Zhu J-M. Prediction and risk assessment of extreme weather events based on gumbel copula function. *J Funct Sp* 2022;2022:1–13.
- [50] Singh VP, Zhang L. IDF curves using the frank archimedean copula. *J Hydrol Eng* 2007;12(6):651–62.
- [51] Demarta S, McNeil AJ. The t copula and related copulas. *Int Stat Rev* 2005;73(1):111–29.
- [52] Charpentier A, Fermanian J-D, Scaillet O. The estimation of copulas: Theory and practice. In: Copulas: From theory to application in finance, vol. 35, Risk Books London; 2007.
- [53] Genest C, Nešlehová J, Quesey J-F. Tests of symmetry for bivariate copulas. *Ann Inst Statist Math* 2012;64:811–34.
- [54] Bedford T, Cooke RM. Vines—a new graphical model for dependent random variables. *Ann Statist* 2002;30(4):1031–68.
- [55] Akaike H. A new look at the statistical model identification. *IEEE Trans Autom Control* 1974;19(6):716–23.
- [56] Du J, Li H, He Y. The method of solving structural reliability with multiparameter correlation problem. *Math Probl Eng* 2017;2017(1):6976301.
- [57] Allahvirdizadeh R, Andersson A, Karoumi R. Improved dynamic design method of ballasted high-speed railway bridges using surrogate-assisted reliability-based design optimization of dependent variables. *Reliab Eng Syst Saf* 2023;238:109406.
- [58] Lebrun R, Dutfoy A. An innovating analysis of the nataf transformation from the copula viewpoint. *Probab Eng Mech* 2009;24(3):312–20.
- [59] Kontolati K, Loukrezis D, Giovanis DG, Vandanaupu L, Shields MD. A survey of unsupervised learning methods for high-dimensional uncertainty quantification in black-box-type problems. *J Comput Phys* 2022;464:111313.
- [60] Blatman G, Sudret B. Adaptive sparse polynomial chaos expansion based on least angle regression. *J Comput Phys* 2011;230(6):2345–67.
- [61] Zhou Y, Lu Z, Yun W. Active sparse polynomial chaos expansion for system reliability analysis. *Reliab Eng Syst Saf* 2020;202:107025.
- [62] Blatman G. Adaptive sparse polynomial chaos expansions for uncertainty propagation and sensitivity analysis (Ph.D. thesis, Clermont-Ferrand 2; 2009.
- [63] Wang F, Li H. System reliability under prescribed marginals and correlations: Are we correct about the effect of correlations? *Reliab Eng Syst Saf* 2018;173:94–104.
- [64] Massey Jr FJ. The Kolmogorov-Smirnov test for goodness of fit. *J Am Stat Assoc* 1951;68–78.
- [65] Chen X, Matsumoto M, Kareem A. Time domain flutter and buffeting response analysis of bridges. *J Eng Mech* 2000;126(1):7–16.
- [66] Jain A, Jones NP, Scanlan RH. Coupled flutter and buffeting analysis of long-span bridges. *J Struct Eng* 1996;122(7):716–25.
- [67] Li S, Li S, Laima S, Li H. Data-driven modeling of bridge buffeting in the time domain using long short-term memory network based on structural health monitoring. *Struct Control Health Monit* 2021;28(8):e2772.